Supplementary Information for

Isothermally Crystallize Perovskites at Room-Temperature

Kai Wang,[1,2*] Congcong Wu,[3] Yuchen Hou,[1] Dong Yang,[1,2] Tao Ye,[1,2*] Jungjin Yoon,[1,2] Mohan Sanghadasa,[4] Shashank Priya[1,2*]

[1] Department of Materials Science and Engineering, Pennsylvania State University, University Park, PA 16802, United States

[2] Materials Research Institute, Pennsylvania State University, University Park, PA 16802, United States

[3] Hubei Collaborative Innovation Center for Advanced Organic Chemical Materials, Key Laboratory for the Green Preparation and Application of Functional Materials, Hubei Key Laboratory of Polymer Materials, School of Materials Science and Engineering, Hubei University, Wuhan 430062, China

[4] U.S. Army Combat Capabilities Development Command Aviation & Missile Center, Redstone Arsenal, Alabama 35898, United States

This PDF file includes:

Supplementary Notes S1 to S6
Figs. S1 to S27
Tables S1 to S5
References (SR1-22)

Supplementary Notes

S1 Summary of low-/mild-temperature synthesized perovskite polycrystalline film

Prior attempts on processing of perovskite thin film with minimal energy / economical budget include the RT-processed film fabrication followed by various post-processing techniques including gas-blowing, antisolvent-washing and mild thermal annealing (TA). We summarize representative prior studies here to show the ongoing progress on low-/mild-temperature processed perovskite thin film for photovoltaic (PV) applications (**Table S1**). All the prior attempts rely on high-boiling-point solvent systems to process the high-quality perovskite polycrystalline thin film. These solvents are DMF, DMSO, NMP, PC, 2-ME, etc., all of which are nonvolatile at RT and require redundant post-processing to remove.

Table S1 Comparison of reported low-/mild-temperature processed perovskite thin films coupled with corresponding device efficiency.

Mechanism	Precursor Solvent System	Temp.	Expense on solvent removing	Time Window	Device Efficiency	Ref.
Gas-blowing	dimethylformamide (DMF, 307.4°F (153°C)) and DMSO	**105 °C**	high N_2 flow rate (42 ± 3 m s^{-1}) + TA @ 105 °C for 60 min	60+ min.	20.26%	[1]
Solvent engineering	Acetonitrile (ACN, bp: 179.6°F (82°C)) + 2-methoxyethanol (2-ME, bp: 255.2°F (124°C))	**100°C**	TA @ 100°C	5-20 min.	16%	[2]
Anti-solvent washing	dimethylsulfoxide (DMSO, bp:372.2°F (189°C)) and γ-butyrolactone (GBL, bp: 399.2°F (204°C))	**90 °C**	Antisolvent + Thermal annealing (TA)	~10 min.	14%	[3]
Two-step-coating + N_2 blow + mild TA	DMF	70 °C	Antisolvent + mild TA @ 70 °C	N/A	11.96%	[4]
Solvent engineering	GBL+ propylene carbonate (PC, bp: 464°F (240°C))	40 °C – **90 °C**	mild TA	N/A	21.90%	[5]
Vacuum evacuation	NMP	N/A	high vacuum (~ 10 mtorr)	3+ min.	8.67%	[6]
Mixed-solvent-vapor annealing	DMF	RT	DMF & antisolvent	12 hrs.	16.40%	[7]

Solvent–Solvent Extraction	N-methyl-2-pyrrolidone (NMP), bp: 395.6°F (202°C)	RT	bath in diethyl ether + N_2 blow	2+ min.	15.20%	[8]
RT isothermal crystallization	Ethanol (EtOH, bp: 173.1°F (78.37°C)) + ACN + amine	RT	N/A	≤ 60 sec.	23.07%	**This work**

S2 Crystallization mechanism study on RT-isothermal synthesized films

The driving force for the precipitation of a solid phase from a supersaturated solution can be quantified by the chemical potential difference ($\Delta\mu = \mu_s - \mu_c$) of a molecule in the solution (μ_s) and crystalline phase (μ_c). Thermodynamically, this can be expressed as:

$$\Delta\mu = kT \ln S \qquad \text{(S1)}$$

where k, T, and S are the Boltzmann constant, absolute temperature, and supersaturation ratio, respectively. Supersaturation is the driving force for crystallization, which can be achieved through *(i) temperature adjustment (cooling*), *(ii) concentration changes (concentrating)*, or by *(iii) altering the solution activity coefficients*, as denoted by the dashed arrow in **Fig. S6A**. The **Fig. S6A** also shows the temperature–composition phase behavior. In this RT-isothermal-crystallized halide perovskite system, the whole process from unsaturated zone (in solution state) to the supersaturated zone (which initiate the crystallization) is driven by the spontaneous solvent evaporation at RT that increases the concentration of the system.

Nucleation

Based on the Classical Nucleation Theory (CNT) (derived from the continuums thermodynamics), the time-dependent nucleation rate can be expressed as:[9]

$$n(t) = \frac{\mathrm{d}N}{\mathrm{d}t} = \frac{N_0 2a}{\mathrm{erfc}(b)\sqrt{\pi}} \frac{\exp[-(\frac{a}{1-\tau}+b)^2]}{(t-\tau)^2} \qquad \textbf{(S2)}$$

where $a = \frac{\xi}{\sqrt{2}\,\sigma_D\,B}$ and $b = \frac{J_m}{\sqrt{2}\,\sigma_D\,B} - \frac{\bar{D}}{\sqrt{2}\,\sigma_D}$, with D and σ_D being the mean and standard deviation of ion vacancy diffusivity for a single population of the breakdown sites on the crystal surface, respectively, J_m is the annihilation flux of cation vacancies, t is time, τ is the dissolution time of the cap over the vacancy condensate from the initial vacancy condensation to the point of rupture, and ξ is the areal concentration of condensed vacancies on the cation sublattice. A general $n(t)$ vs. t plot is shown in **Fig. S6B**. The nucleation rate $n(t)$ firstly displays an increase, followed by a peak of maximal rate and then a decrease. Here in this work, we found the nucleation process of the RT-crystallized halide perovskite also followed this classical nucleation mechanism. Specifically, we monitored the nucleation process in a RT-isothermal condition and took snapshots at different time to count the nucleuses. **Fig. S7A** shows the snapshots of optical microscopic images frozen at different time during the nucleation process. We then calculate the nuclei density by counting the nuclei numbers in a specific region at different time and plot the nuclei density-time curve in **Fig. S7B**. By taking the first order derivative, we can obtain the $n(t)$ vs. t plot in

Fig. S7 C. Clearly, the $n(t)$ vs. t plot for the RT-crystalized $MAPb(I_{1-x}Cl_x)_3$ exhibit similar feature to the classical theory, displaying three regions of diffusion-control, nucleation, and growth.

Crystal growth

The *in-situ* study on the crystal growth of the $MAPb(I_{1-x}Cl_x)_3$ was performed on an optical microscopy at room temperature (with a RH of 43%) in ambient atmosphere. The growth process was recorded in **Supplementary Video 4 (SV 4_In-situ OM Observation)** and snapshots at different time are shown in **Fig. S8A**. We measure the radius (r_t) of a crystal at each time t, and take the ratio of r_t/r_f with r_f being the radius of the crystal at the final state. **Fig. S8B** shows the plot of r_t/r_f *vs.* t. The r_t/r_f corresponds to the volumetric crystalline phase fraction of the instant crystal to the final crystal. The volume fraction dependence on crystalline phase and crystallizing time can be described by the Avrami equation as:[10]

$$\mathrm{V}(t) = 1 - \exp(-kt^n) \qquad \text{(S3)}$$

where $\mathrm{V}(t)$ is the ratio between crystalline phase at time t to that at equilibrium state (v/v). $\mathrm{V}(t)$ can be determined by:

$$\mathrm{V}(t) = \frac{V_c(t)}{V_c(\infty)} = \frac{\int q(t)dt}{\int_0^\infty q(t)dt} \qquad \textbf{(S4)}$$

where k is a constant corresponding to the rate of reaction and is dependent on the molecular weight and crystallization temperature (T_{crys}), and n is the Avrami exponent for a certain material and can be influenced by the nucleation kinetics. Avrami equation is developed for the isothermal conditions and could be used in the condition of constant temperature, which is used here to reveal the kinetic nature of the crystallization of the material. The interpretation of Avrami constants provides understanding of the underlying physics during the crystallization process. To obtain the Avrami constants, we take logarithm on both sides of **Equation S3** to get:

$$\ln\big(1 - V(t)\big) = -kt^n \qquad \textbf{(S5)}$$

Further taking logarithm on both sides of **Equation S5**, we can obtain:

$$\log(-\ln\big(1 - V(t)\big)) = \log(k) + n \cdot \log(t) \qquad \textbf{(S6)}$$

In this way, by plotting $\log(-\ln\big(1 - V(t)\big))$ vs $\log(t)$, we can get Avrami constants of n from the slope and k from the *y*-axis intercept. **Fig. S8C** shows the plot of $\log(-\ln\big(1 - V(t)\big))$ *vs.* $\log(t)$. By extracting the slope and intercept, we obtained the constants of n = 3.63 and k = 7.6×10^{-7}, respectively. The Avrami exponent (n) consists of two terms given by equation:

$$n = N + C \qquad \textbf{(S7)}$$

where nucleation parameter (N) is either 0 or 1 and crystallization (C) is 1, 2 or 3 (denoting growth dimension). In this study, we found n = 3.63 > 3, which suggests that the crystal growth involves a three-dimensional growth accompanied by a simultaneous nucleation process. The three-dimensional growth assists the crystal grain growth to a size of hundreds of nanometers in the thin film in **Fig. 1 in the main text**. The nucleation is also involved during the process, which can be understood by the fast solvent evaporation that leads to the supersaturation of the system. Overall, nucleation can be random and growth unhindered leading to high values for $3 < n < 4$.

S3 Structural identification of perovskite intermediate of $MA(A)_nPb(I_{1-x}Cl_x)_3$

Powder X-ray diffractions of perovskite intermediate crystal and Rietveld refinement

To characterize the phase of the perovskite intermediate crystal ($MA(A)_nPb(I_{1-x}C_{lx})_3$, n>1, as shown in a picture in **fig. S13**), single crystals were grounded thoroughly in an agate mortar in a chamber filled with amine atmosphere and quickly transferred for measurement using powder X-ray diffraction (PXRD). The PXRD spectra was recorded in **fig. S14E**. Rietveld structure refinement was performed by using the PXRD data and a constructed unit cell model (**fig. S14F**). The final refined results of unit cell parameters and reliability factors for as-grown $MA(A)_nPb(I_{1-x}C_{lx})_3$ are listed in **Table S2**. The strong $\{00\ell\}$ orientations of thin films of $MA(A)_nPb(I_{1-x}C_{lx})_3$ intermediate perovskite and final $MAPb(I_{1-x}C_{lx})_3$ perovskite are also confirmed by XRD analysis in **fig. S14D** and **fig. S16**, respectively.

Table S2 Crystallographic data for $MA(A)_nPb(I_{1-x}C_{lx})_3$ crystal based on Rietveld refinement.

Cell parameters	**a/b (Å)**	**c (Å)**	**α (°)**	**β (°)**	**γ (°)**
	8.81532(11)	24.66372 (4)	90	90	90
Space group		p b c a			
Unit-cell volume		1916.41 ($Å^3$)			
R_{wp} (%)		8.75			
R_p (%)		11.58			
χ^2		0.1224			
Atomic coordinates	X	Y	Z	Occ.	U
H1	0.8170	0.7720	0.7303	1	0.069
H2	0.9968	0.7484	0.7459	1	0.069
C3	0.8890	0.7560	0.7590	1	0.046
H4	0.8815	0.8387	0.7822	1	0.069
N5	0.8460	0.6180	0.7849	1	0.042
H6	0.7363	0.6246	0.7969	1	0.051
H7	0.9570	0.4870	0.8340	1	0.038
H8	0.9508	0.3574	0.8342	1	0.040
H9	0.9448	0.6002	0.7905	1	0.045
C10	0.9250	0.4400	0.8573	1	0.033
H11	0.8115	0.4325	0.8657	1	0.040
I12	1.0779	1.0298	0.8822	1	0.031
H13	1.1198	0.4326	0.8947	1	0.045
N14	1.0160	0.4270	0.9025	1	0.030
H15	0.9957	0.3391	0.9175	1	0.045
H16	0.9905	0.5015	0.9239	1	0.045
I17	0.6987	1.2042	0.9771	1	0.031
Pb18	1.0000	1.0000	1.0000	1	0.024

S4 Photo-carrier diffusion length quantification through PL study

We use the PL study and a diffusion model (referring to previous reports [11,12]) coupled with continuum theory to calculate the photo-carrier diffusion length in perovskite thin film. Briefly,

consider the photoactive perovskite layer with a film thickness of L. Such a layer will be further coated by either a photocarrier blocking or a quenching layer. We define a length of x as a distance away from the sample surface upon incident light. A generalized diffusion equation can be written using the continuum theory as:

$$\frac{\partial n(\mathbf{r},t)}{\partial t} = \boldsymbol{\nabla} \cdot [D(n,\mathbf{r},t)\boldsymbol{\nabla} n(\mathbf{r},t)] - \frac{n(\mathbf{r},t)}{\tau} + G(\mathbf{r},t) \qquad \text{(S8)}$$

where $n(\mathbf{r},t)$ is the local density, τ is the lifetime of photocarriers, $D(n,\mathbf{r},t)$ is the diffusion coefficient, and $G(\mathbf{r},t)$ the generation rate, respectively. In the case of a bi-layer structure, the spatial distribution is one-dimensional (1D) for these photocarriers. Thus, we can obtain $n(\mathbf{r},t) = n(x,t)$, where x is the distance from the sample surface upon illumination. Under assumption of low photo-carrier density, there will be no high-order carrier-carrier interaction and the diffusivity is assumed to be independent of either the carrier density or the position inside the homogeneous film, i.e., $D(n,\mathbf{r},t) = D(t)$. Under these approximations, **Equation S8** can be simplified as:

$$\frac{\partial n(x,t)}{\partial t} = D(t)\frac{\partial^2 n(x,t)}{\partial x^2} - \frac{n(x,t)}{\tau} + G(x,t) \qquad \text{(S8*)}$$

Now we consider the initial distribution of photo-carrier under an instantaneous photon-excitation. At the initial-state the net-generation rate ($G(\mathbf{r},t)$) can be omitted. We can obtain an initial-state charge distribution term as [13]:

$$n(x,0) = G(x) = n_0 \exp(-\frac{\alpha x}{\cos\theta}) \qquad \text{(S9)}$$

where n_0 is a constant related to the laser light, α is the absorption coefficient at the excitation wavelength, θ is the incidence angle of the laser pulse with respect to the out-of-plane direction of the film sample surface, respectively. Following, we will consider three cases of *(i) ideal case of quenching, (ii) absence of quencher, and (iii) thickness-dependent transient quenching*.

*(i) In the **ideal case of quenching**:*

Applying the boundary condition at $x = 0$ (blocking by surface, i.e., no diffusion or quenching), we have

$$\frac{\partial n(0,t)}{\partial x} = 0 \qquad \text{(S10)}$$

At $x = L$ (quenching by a bottom quenching layer and thus no photo-carriers), we have

$$n(L,t) = 0 \qquad \text{(S10*)}$$

By solving Equations from S8* to S10*, the solution of photo-carrier density distribution ($n(x,t)$) is function of position x and time t , which can be written as:

$$n(x,t) = n_0 \sum_{k=0}^{\infty} A_k \exp[-\left(\frac{1}{\tau} + {B_k}^2 \frac{D}{L^2}\right) t] \cos(B_k \frac{x}{L}) \qquad \text{(S11)}$$

where parameters A_k and B_k have the following expressions:

$$A_k = \frac{2\left[B_k(-1)^k \exp\left(-\frac{\alpha L}{\cos\theta}\right)+\frac{\alpha L}{\cos\theta}\right]}{{B_k}^2+(\frac{\alpha L}{\cos\theta})^2} \qquad \textbf{(S11*)}$$

$$B_k = (k+\frac{1}{2})\pi \qquad \textbf{(S11**)}$$

with k being natural number with value of $0, 1, 2, ...$ (using a finite Fourier transform method [14]). Since the photo-carrier diffusion length is proportional to the square root of the mobility and carrier lifetime [15], in 1D diffusion model we have:

$$L_D \equiv \sqrt{2D\tau} \qquad \textbf{(S12)}$$

Here the L_D is the minimum 1D net displacement achieved by $1/e$ of the initial population of photo-carriers. In terms of L_D, **Equation S11** can be transformed as:

$$n(x,t) = n_0 \sum_{k=0}^{\infty} A_k \exp\left\{-\frac{t}{\tau}\left[1+\frac{{B_k}^2}{2}\left(\frac{L_D}{L}\right)^2\right]\right\}\cos(B_k\frac{x}{L}) \qquad \textbf{(S11***)}$$

in dependence of a dimensionless parameter of $\frac{L_D}{L}$, denoting the ratio between the length of diffusion and the film thickness (L).

(ii) *In the case of* ***absence of quencher***:

There is no quenching layer and the perovskite layer has both sides "blocking". Applying the boundary condition at $x = L$, we have

$$\frac{\partial n(L,t)}{\partial x} = 0 \qquad \textbf{(S12)}$$

By solving **Equations** from **S8*** to **S10** coupled by **S12**, we have

$$n(x,t) = n_0 A_0 \exp\left(-\frac{t}{\tau}\right) + n_0 \sum_{k=1}^{\infty} A_k \exp\left\{-\frac{t}{\tau}\left[1+\frac{{B_k}^2}{2}\left(\frac{L_D}{L}\right)^2\right]\right\}\cos(B_k\frac{x}{L}) \qquad \textbf{(S13)}$$

where parameters of A_0, A_k and B_k have the following expressions:

$$A_0 = \frac{\cos\theta}{\alpha L}\left[1-\exp\left(-\frac{\alpha L}{\cos\theta}\right)\right] \qquad \textbf{(S13*)}$$

$$A_k = \frac{\frac{2\alpha L}{\cos\theta}\left[1-(-1)^k\exp\left(-\frac{\alpha L}{\cos\theta}\right)\right]}{{B_k}^2+\left(\frac{\alpha L}{\cos\theta}\right)^2} \qquad \textbf{(S13**)}$$

$$B_k = k\pi \qquad \textbf{(S13***)}$$

with k being natural number of $0, 1, 2, ...$

(iii) *In the case of thickness-dependent* ***transient quenching****:*

The average photo-carrier lifetime in dependence of L_D/L and native lifetime can be obtained based on above derivation and has the following expression:

$$\bar{n}(t) = n_0 \sum_{k=0}^{\infty} A_k \exp\left\{-\frac{t}{\tau}\left[1+\frac{{B_k}^2}{2}\left(\frac{L_D}{L}\right)^2\right]\right\} \qquad \textbf{(S14)}$$

where

$$A_k = \frac{2\left[B_k \exp\left(-\frac{\alpha L}{\cos\theta}\right)+(-1)^k \frac{\alpha L}{\cos\theta}\right]}{B_k\left[{B_k}^2+\left(\frac{\alpha L}{\cos\theta}\right)^2\right]} \qquad \textbf{(S14*)}$$

$$B_k = \left(k+\frac{1}{2}\right)\pi \qquad \textbf{(S14**)}$$

with k being natural numbers of $0, 1, 2, ...$

This **Equation S14** can also be regarded as a sum of multiple exponential terms, each weighted by $n_0 A_k$ with a decay rate of

$$\tau_k = \tau\left[1+\frac{{B_k}^2}{2}\left(\frac{L_D}{L}\right)^2\right]^{-1} \qquad \textbf{(S15)}$$

In this way, we can rewrite **Equation S14** to be

$$\bar{n}(t) = n_0 \sum_{k=0}^{\infty} A_k \exp\left(-\frac{t}{\tau_k}\right) \qquad \textbf{(S16)}$$

By comparing the PL lifetime in presence and absence of the quenching layer, the photo-carrier diffusion length (L_D) can be calculated based on the limit behavior of the infinite series solution of **Equation S16**. It should be noted that above equations were derived based on the fact that the quenching interface is opposite to side of laser incidence. From **Equations S14** to **S16**, the coefficient A_k, defined as the weight of each term in the infinite series of $\bar{n}(t)$, correlates to the optical depth of the photoactive layer. A qualified measurement requires the film thickness less than the attenuation length, i.e., $\alpha L < 1$. Specifically, for this study we use perovskite thin film with a thickness of 180 nm under an excitation wavelength of 650 nm (α=5.4×10^4 cm^{-1}), which is in accordance to this assumption. Overall, in these conditions the first term A_0 is more than 80 % (for numerical approximation of the order of error) of the sum of all of the remaining coefficients. We can make approximation of **Equation S16** to be

$$\bar{n}(t) \cong n_0 A_0 \exp\left(-\frac{t}{\tau_q}\right) \qquad \textbf{(S17)}$$

where the average photo-carrier lifetime (τ_q) in presence of a quencher is defined by

$$\tau_q \equiv \tau\left[1+\frac{\pi^2}{8}\left(\frac{L_D}{L}\right)^2\right]^{-1} \qquad \textbf{(S18)}$$

By solving **Equation S18**, we can obtain the photo-carrier diffusion length (L_D) by

$$\frac{L_D}{L} = \frac{2\sqrt{2}}{\pi}\sqrt{\frac{1}{\tau_q/\tau}-1} \qquad \textbf{(S19)}$$

It should be noted that above derivation is under assumption of instantaneous photoexcitation, which is applicable for this study because the timescale of photo-carrier transport and decay in the perovskite thin films (with a μs scale) is much longer than the temporal width of the laser pulse.

Otherwise, modification terms such as convolution with the instrument response function (IRF) needs to be added, which is applied to the cases of perovskite films coated with quenching layers.

S5 Discussion on driving force of amine releasing

The evaporation of liquid towards gas phase is spontaneous if the surrounding temperature is higher than the boiling point of the liquid (assuming standard pressure). This is driven by the difference of Gibbs free energy ($\Delta G_0 < 0$) between the gas and liquid state. In a solution system, additional interaction between the volatile molecules and the other molecules within the system could add a "resistive force" against the evaporation of these volatile molecules. Or an additional contribution to the original ΔG_0, making the overall ΔG_0 might not be < 0. In the case of the RT-ink system, taking MA as an example, the MA has a low boiling point (bp) of -6°C so that the ΔG_0 could be negatively large (easy evaporation). While on the other side, MA also has certain interactions with the octahedral cage (e.g., hydrogen bond), so that there is a competition between the "MA-evaporating (driven by the Gibbs energy difference of MA itself at gas and liquid phase)" and "MA-anchoring (by the octahedral cage to MA)". In another word, the overall Gibbs energy difference now has an additional positive contribution from the "MA-anchoring" (as expressed by the Equation shown below) that resists the evaporation.

Pure MA: $\Delta G_0 = G_{gas}(final\ state) - G_{liquid}(initial\ state)$

MA in RT-ink: $\Delta G_1 = G_{gas}(final\ state) - (G_{liquid} + G_{effective\ anchoring\ contribution})\ (initial\ state) = (G_{gas} - G_{liquid}) - G_{effective\ anchoring\ contribution} = \Delta G_0(drive) - G_{effective\ anchoring\ contribution}(resist)$

When $\Delta G < 0$, the phase transition occurs. This happens to low bp amine such as MA. In terms of high bp amine such as PA (bp: 49°C), additional thermal energy would be required to thermally trigger the release of these PA molecules into evaporation.

S6 Discussion on non-ionicity of the RT-ink

The conventional ink solution (TA-ink) usually dissolves free ions (Pb^{2+}, MA^{+}, I^{-}) in the high-bp (boiling point) solvents. The crystallization of TA-ink starts from the assembly of these disordered free ions into ordered crystals. In comparison, the ink (RT-ink) we develop in this study contains the intermediate state that has less mobile free ions in the low-bp solvents. Comparing the TA-ink and RT-ink, there are two major differences: (i) the 'solute' and (ii) the 'solvent'. The solute in TA-ink is free mobile ions having dynamic movement in the ink; while the 'solute' in RT-ink is the intermediate/transitional states (molecules are already assembled in certain degree and are more ordered than the free ions in the TA-ink) that can quickly jump into the final β-phase (black)

perovskite upon solvent evaporation (driven by Gibbs energy difference of the between gas and liquid phase of amine or the amine's tendency to evaporation). The low-bp solvents in RT-ink secures the fast evaporation and hence the annealing-free feature.

In terms of the concern that why such a high-quality crystal grows in such a short time, it should be related to the difference of 'solute' states between the TA- and RT- inks. Briefly, TA-ink contains mobile free ions in high-bp solvents. The large amount of these free ions represents a highly disordered state. The assembly of these free ions into a highly ordered crystal need more time and energy to rotate, re-orientate, and assembly individual free ions into the crystal. Otherwise a short time will cause defects in the final crystal. For such conventional TA-ink, normally a slower crystal growth could provide sufficient time for those re-orientation and re-alignment of ions and hence less defects in the crystal. However, in the case of the RT-ink, the process is different. The RT-ink contains a relatively more ordered intermediate cluster (compared to the TA-ink) and less free ions (confirmed in **Figs. 1E&F**). Transition from these intermediate ('semi-final') states to the final sates would be easier and more time-efficient compared to the 'free ions – to – crystal' transition in TA-ink, as those sub-dynamic changes such as individual ions' re-orientation/re-alignment are excluded in the transition in RT-ink and the ions are already assembled within the intermediate sate. Meanwhile, the intermediate is a metastable transitional state, higher free energy than that of TA-ink. The TA-ink needs to overcome an energy barrier to proceed the transition, where higher temperature is typically needed to remove solvent and the provide the thermal energy to overcome barriers during molecular assembly. In comparison, the 'intermediate –to– crystal' transition between the RT-ink to the final crystal is more favorable.

To verify the nature of minimized ions in the RT-ink, we compare the ionic current in different inks by using these inks as electrolyte under a cyclic voltammetry measurement. As can be seen in **Fig. 1F**, the TA-ink shows an ionic current over 200 μA under 0.4 V, which is over three-order-magnitude larger than that of 100 nA from the RT-ink (**Fig. 1E**). This indicates a significantly lower concentration of ions in the RT-ink. In addition, we also execute an electrolytic cell test. Both inks are supplied by a 1.5 V DC bias for 5 hr. As can be seen in the photography inserted in **Fig. 1F**, the color of the TA-ink turns into orange due to the precipitation of I_2. And at the cathode, there are precipitation of lead. This result verifies the existence of free I^- and Pb^{2+} in the original TA-ink which can experience a redox reaction under external bias. In contrast, the RT-ink does not show such observation, as it contains already assembled molecules and there is minimized free ions in the system. Overall, the RT-ink and TA-ink are different in nature in terms of 'solute'.

Briefly, both the difference in 'solute' and 'solvent' between the RT-ink and TA-ink makes each crystallization process follows different routes: TA-ink needs long time to get high-quality crystal while the RT-ink does not necessarily need the long time but can get the high-quality crystal as well.

Supplementary Figures

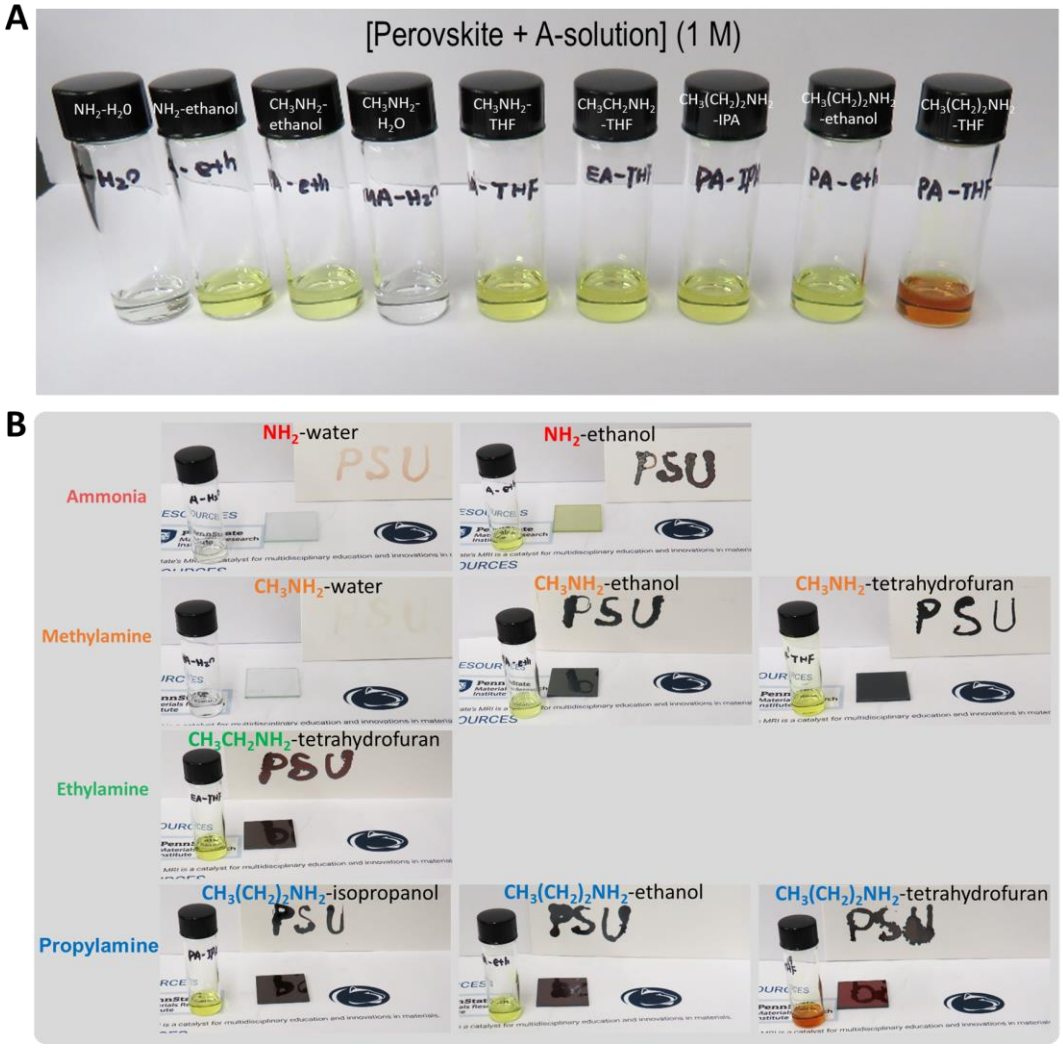

fig. S1 Photograph of multiple amine-based RT-ink. (A) Photograph showing different amine-based inks. (B) Photograph showing different RT-inks and their corresponding writing and RT-perovskite thin film results. All the solutions are prepared by dispersing perovskite crystals into a mixture solution of (1) amine (could be ammonia (NH_2), methylamine (CH_3NH_2) and propylamine ($CH_3(CH_2)_2NH_2$), etc.,), (2) a volatile solvent (could be water, ethanol, isopropanol, tetrahydrofuran, etc.), and (3) acetonitrile. The final concentration of perovskite and amine is 1.2 M and 4.8 M, respectively. The volume ratio between volatile solvent and acetonitrile is 6:4.

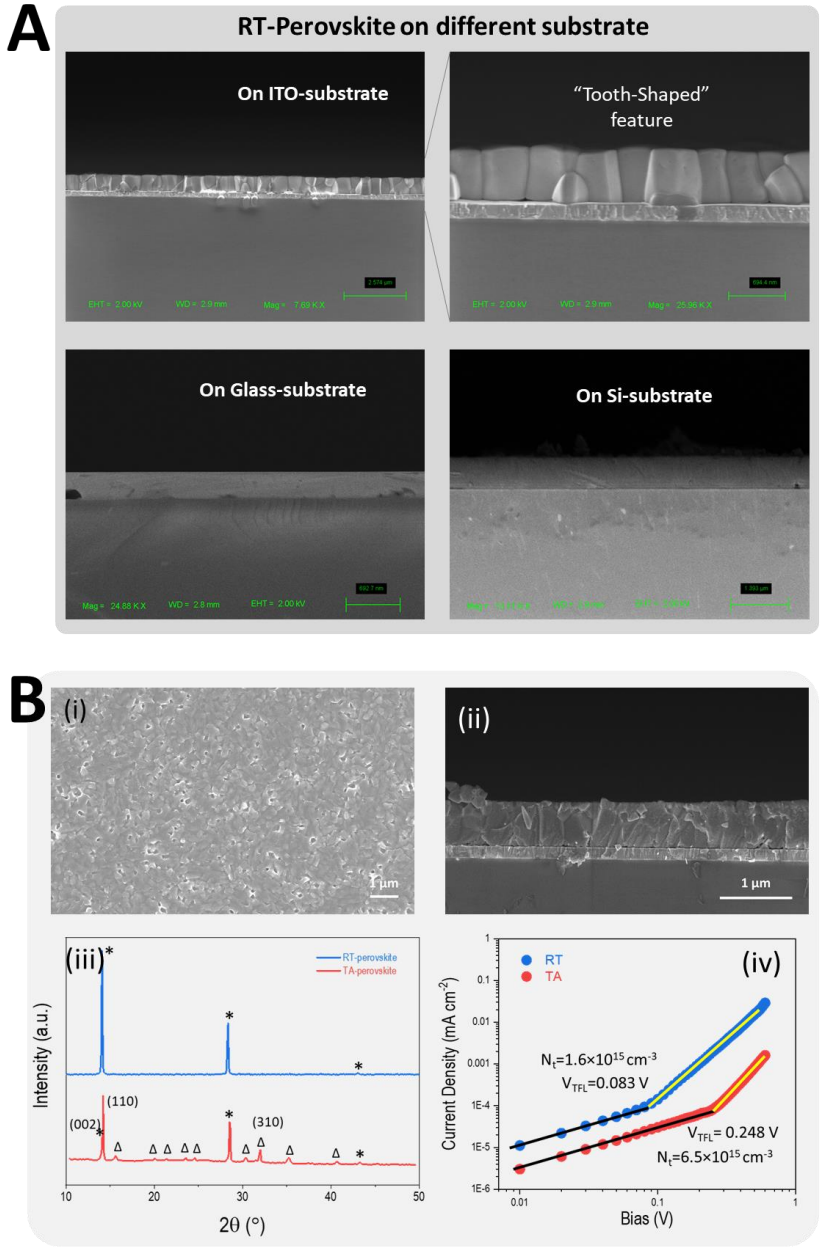

fig. S2 (A) Cross-sectional images of RT-perovskite on different substrates. There is a high-level uniformity for the resultant RT-perovskite thin films. The RT-ink can crystalize quickly in any substrate, even directly writing on a paper. In terms of the crystals, there could be slight difference (e.g., the tooth-shape shown above). These could be related to the surface roughness and surface energy of different substrates, which could tune the crystallization in certain level. Nevertheless, the resultant film on different substrate has compact and uniform feature. **(B)** (i) Top-view, (ii) cross-sectional SEM of TA-perovskite, (iii) its XRD spectrum in comparison with that of a RT-perovskite ('*' denotes the {00 ℓ} planes, 'Δ' denotes other plane sets. The TA-perovskite exhibit less aligned scattering feature compared to the RT-perovskite) and its trap-density estimation *vs.* RT-film (using a hole only device of FTO/PEDOT:PSS/perovskite/Spiro-OMeTAD/Au and corresponding J-V curve measured in dark).

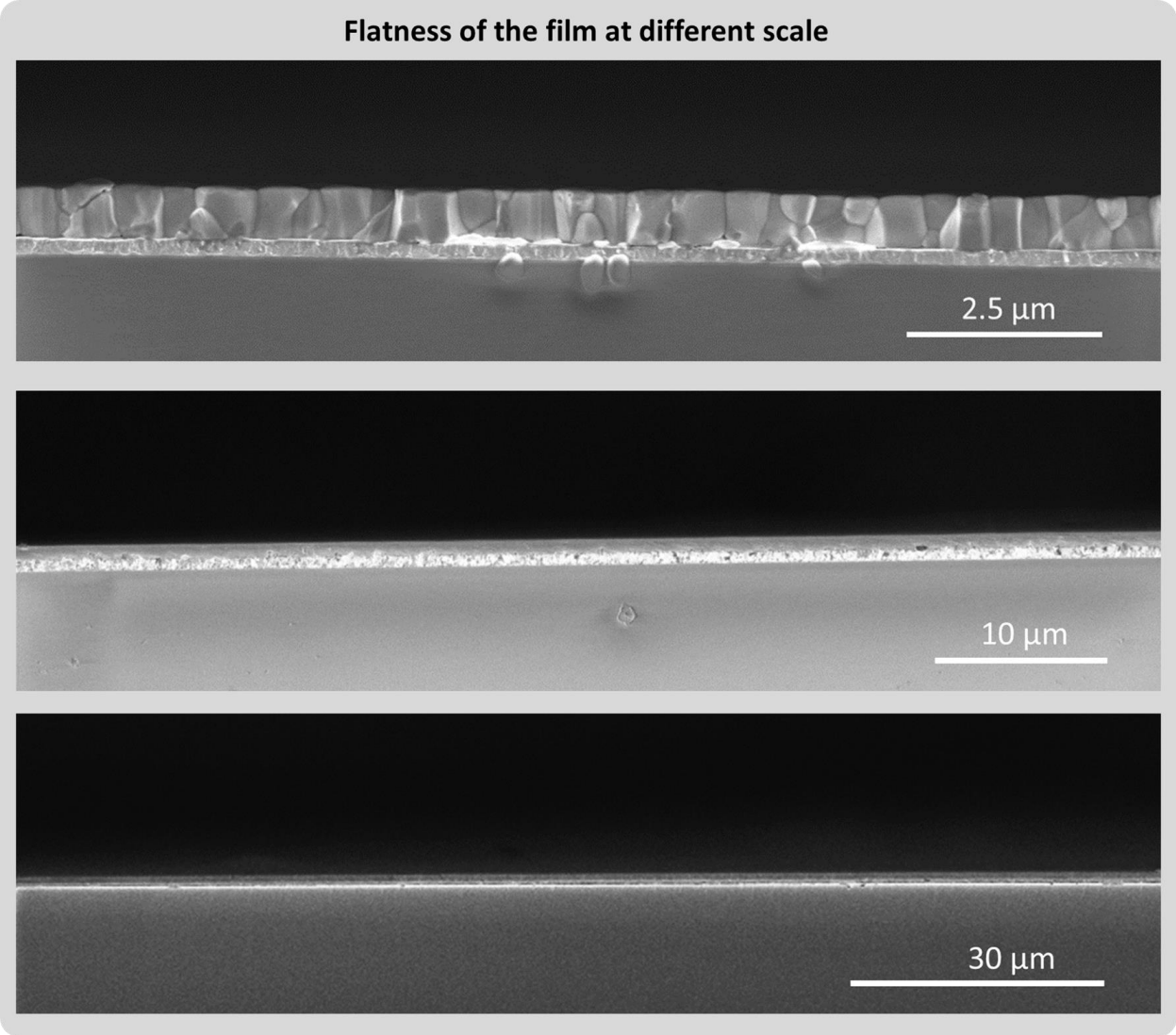

fig. S3 Larger scale cross-sectional SEM images of RT-perovskite thin film showing good film surface flatness and thickness uniformity.

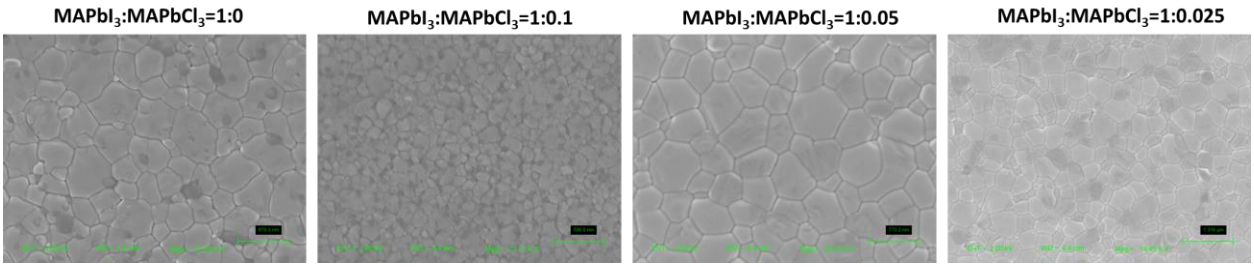

fig. S4 SEM images of RT-perovskite thin films with incorporation of chloride with different ratios.

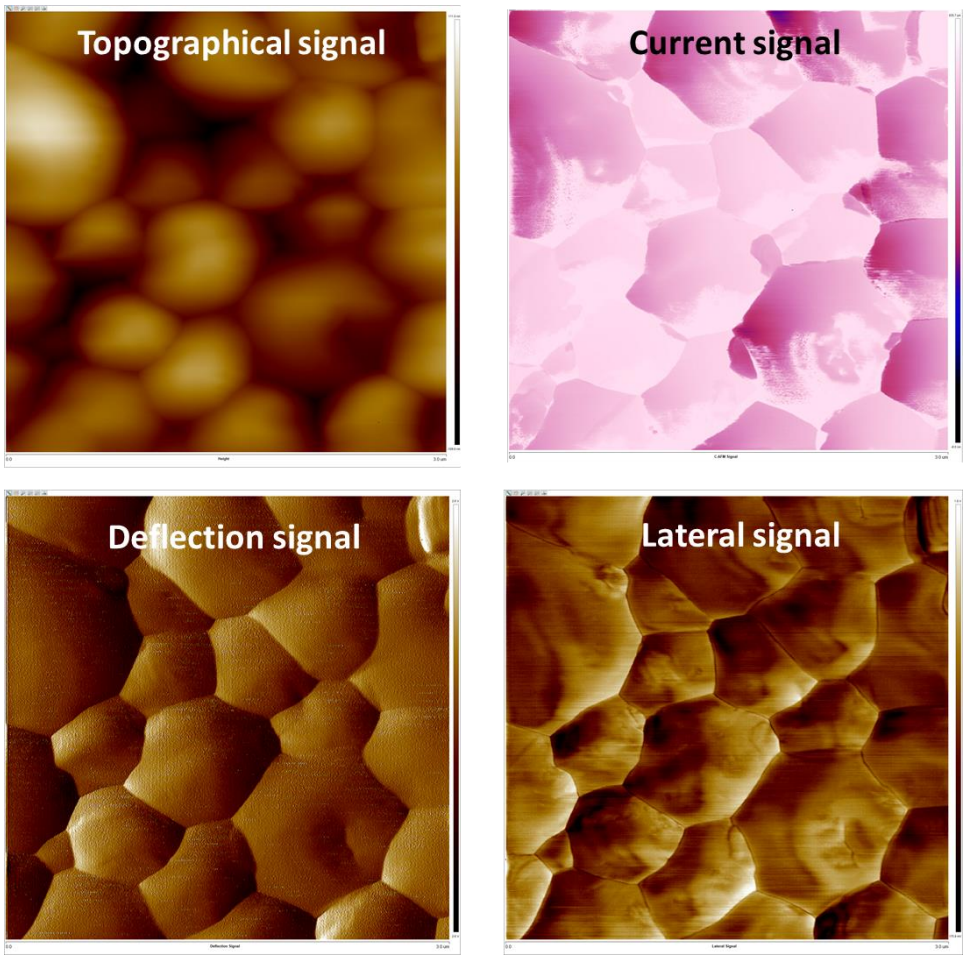

fig. S5 RT-perovskite thin film surface morphology and corresponding surface properties characterized by C-AFM measurement. Grain size is consistent to SEM results and the current map shows a good electrical uniformity of the film.

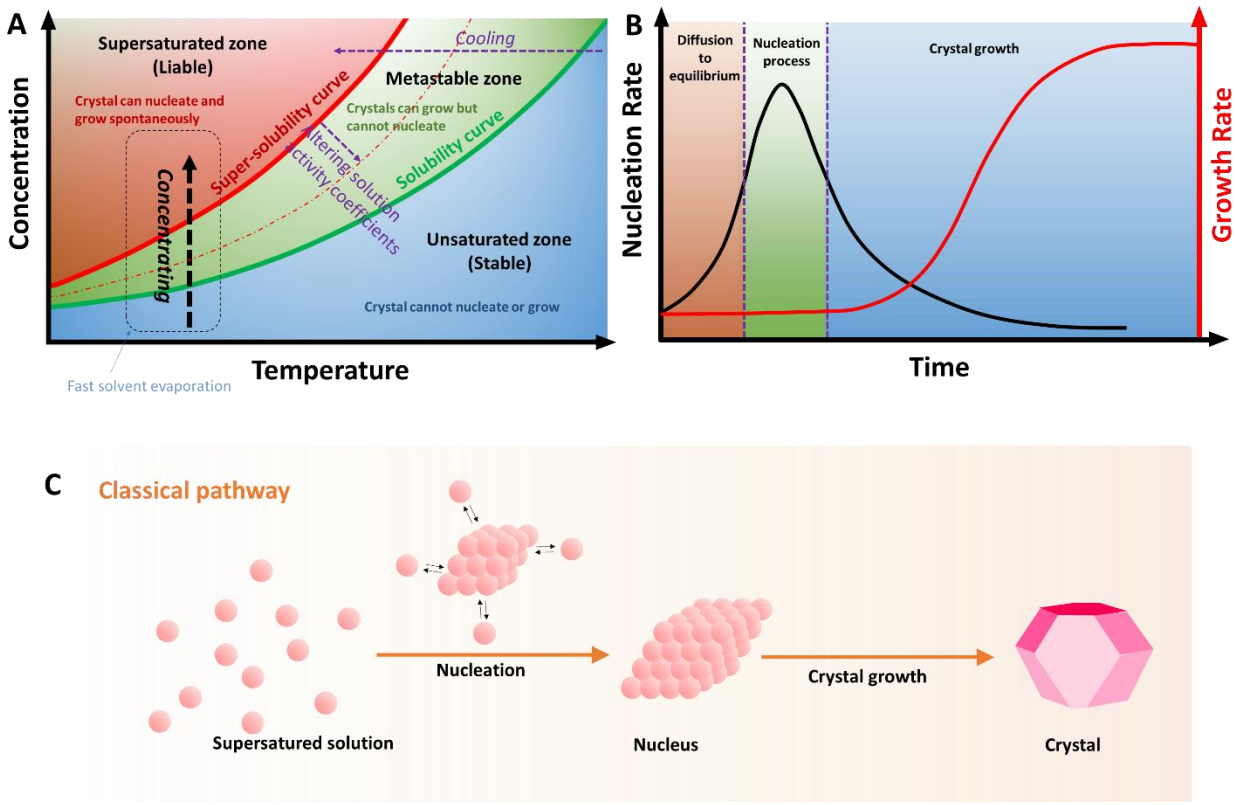

fig. S6 Crystallization theory. (A) Solubility curve and metastable zone plotted against temperature and concentration. Adapted from ref. [16]. **(B)** Time dependence of nucleation rate (according to the Classical Nucleation Theory (CNT)) and growth rate. **(C)** Schematic illustration of the classical pathway of molecular assembly during the crystallization process. Adapted from ref. [17].

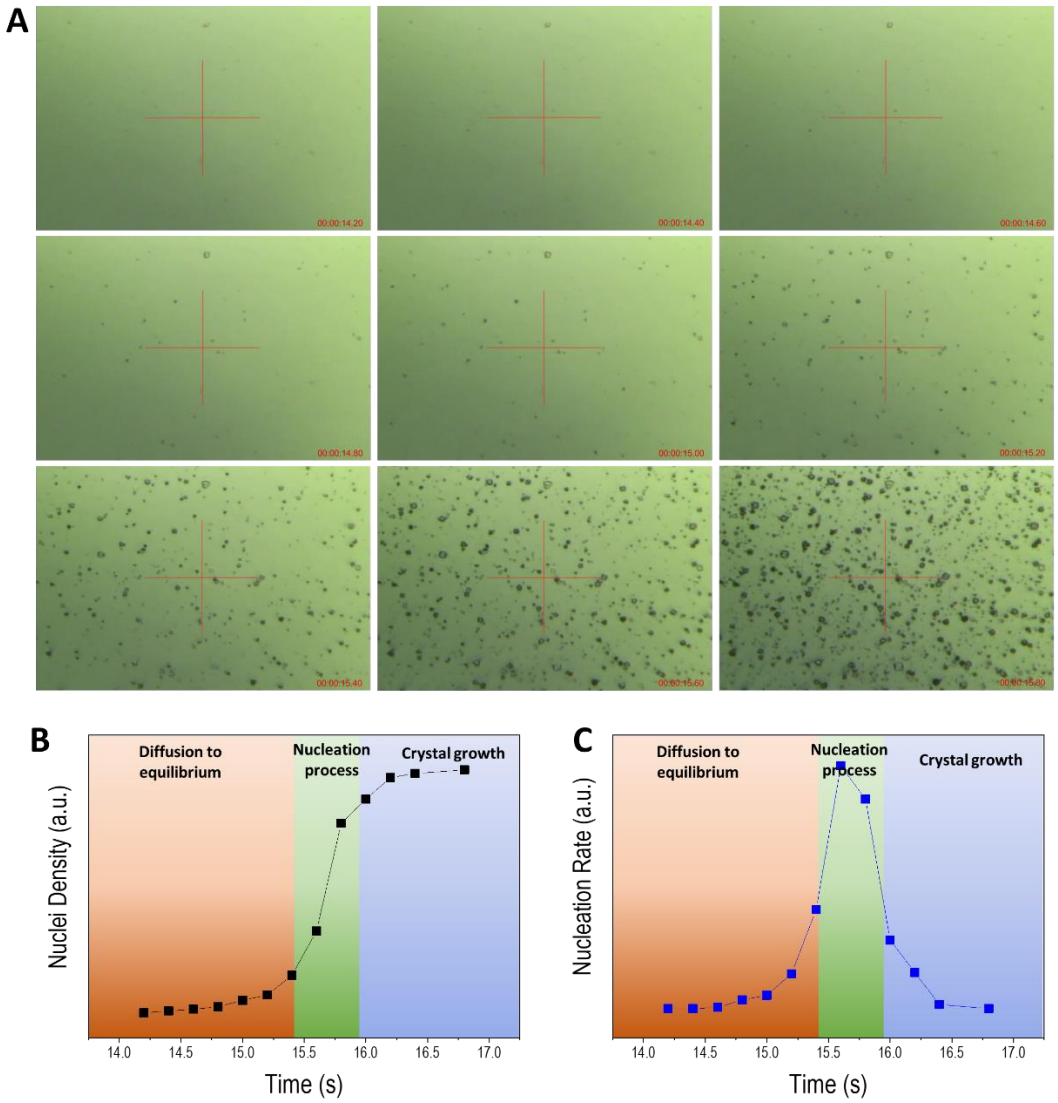

fig. S7 *in-situ* study on the nucleation of the $MAPb(I_{1-x}Cl_x)_3$. (A) Snapshots of optical microscopic images on the nucleation at different time. **(B)** Nuclei density (obtained from counting the nuclei numbers in a specific region) vs. time. **(C)** The first derivative of nuclei density-time plot, which corresponds to the nucleation rate vs. time.

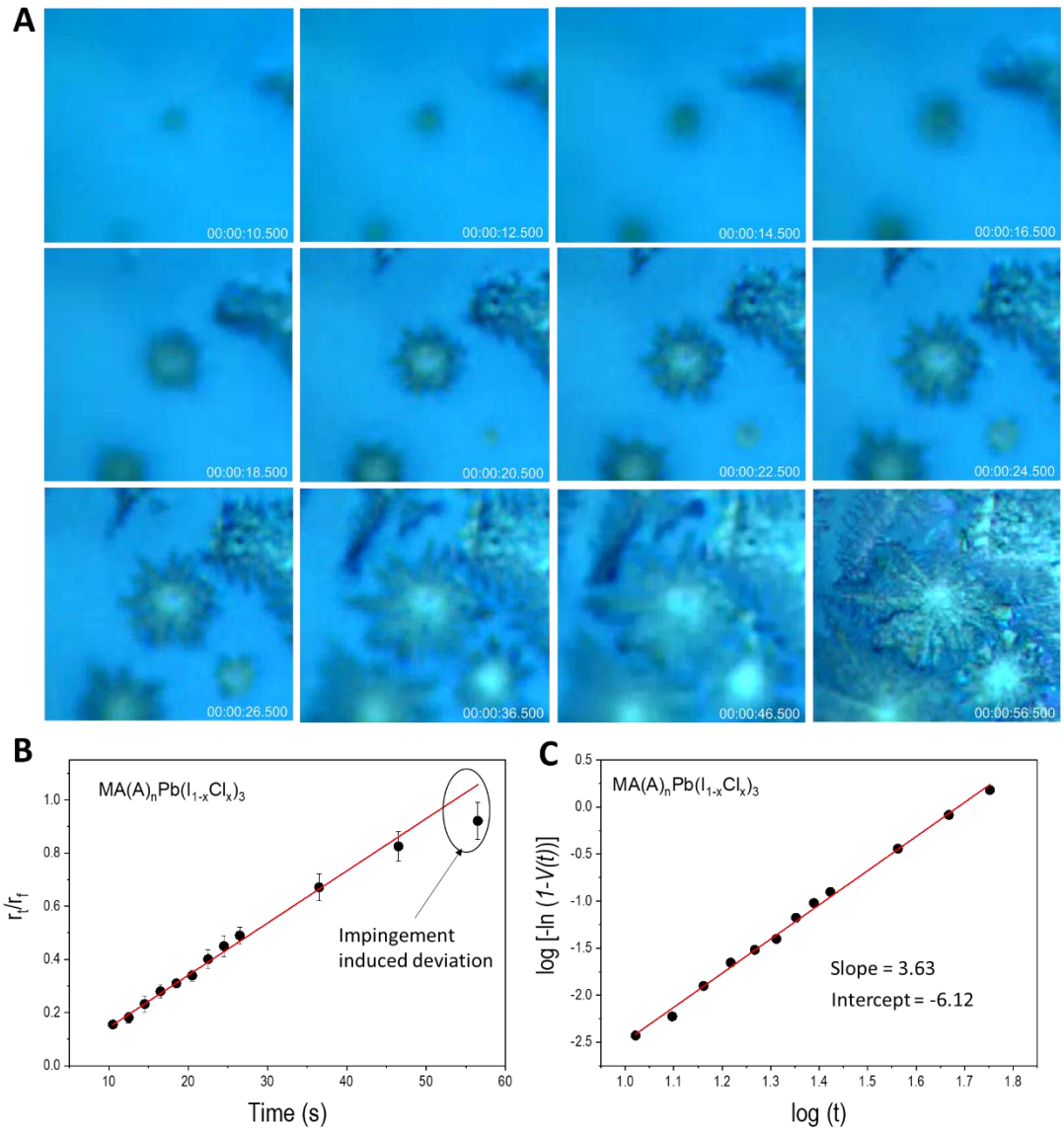

fig. S8 *in-situ* study on the crystal growth of the $MAPb(I_{1-x}Cl_x)_3$. (A) Snapshots of optical microscopic images on a growing crystal at different time. **(B)** Plot of r_t/r_f *vs.* t, where the instant radius is measured at each time on the optical image by using imageJ software. **(C)** Plot of $\log(-\ln(1-V(t)))$ *vs.* $\log(t)$ to investigate the Avrami constants.

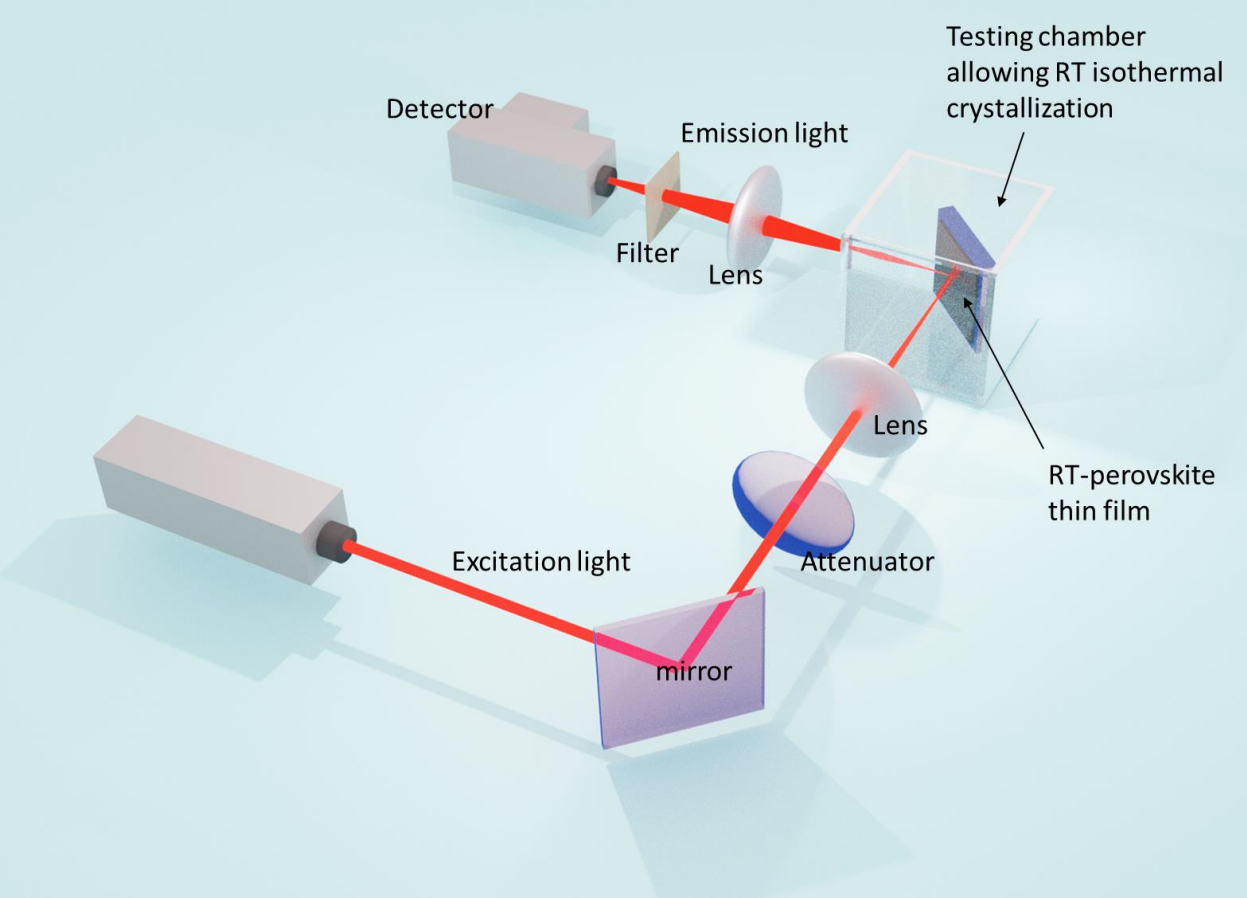

fig. S9 Schematic of *in-situ* PL tracing during the RT isothermal crystallization process. A homemade chamber is utilized to decelerate the crystallization process through filling the volatile gas component identical to those in the RT-ink such that increase their saturate pressure and mitigate their evaporation rate.

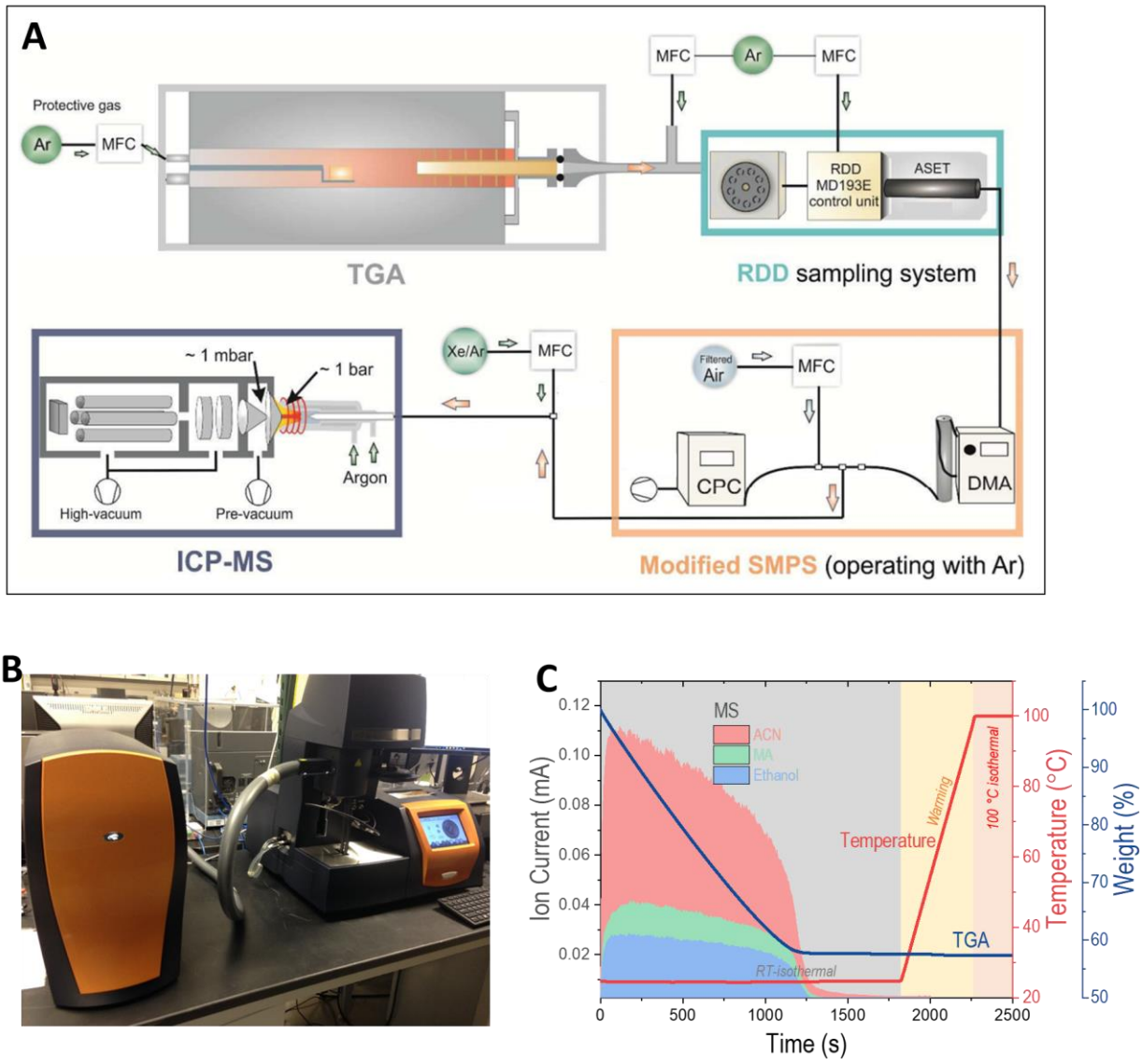

fig. S10 TGA-MS measurement on the RT isothermal crystallization process of perovskite. (A) Setup scheme showing the online analysis of mass spectrometry (MS) coupled thermogravimetric analyzer (TGA), adapted from ref. [18]. (B) Photograph of the Discovery Series TGA-MS is a thermogravimetric analyzer coupled with a Mass Spectrometer used in this study. (C) The TGA/MS data result of RT isothermal crystallization of perovskite.

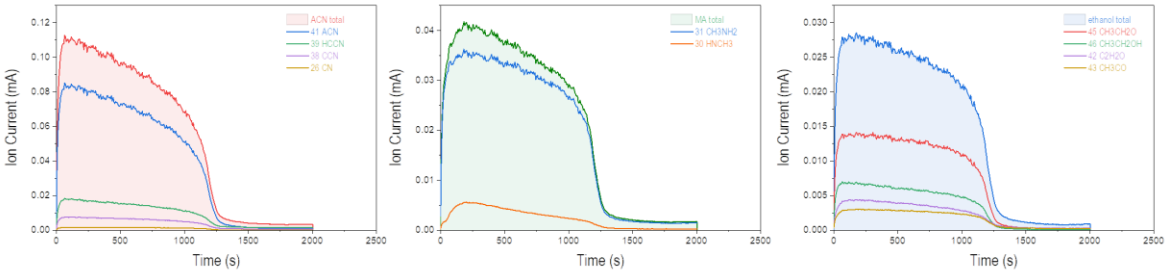

fig. S11 Ion current vs. time plot to identify the chemical composition of evaporated component, according to the chemical fragment characterized by the MS. For the RT-perovskite, there are three components coming from the RT-ink during the spontaneous crystallization process: acetonitrile, methylamine and ethanol.

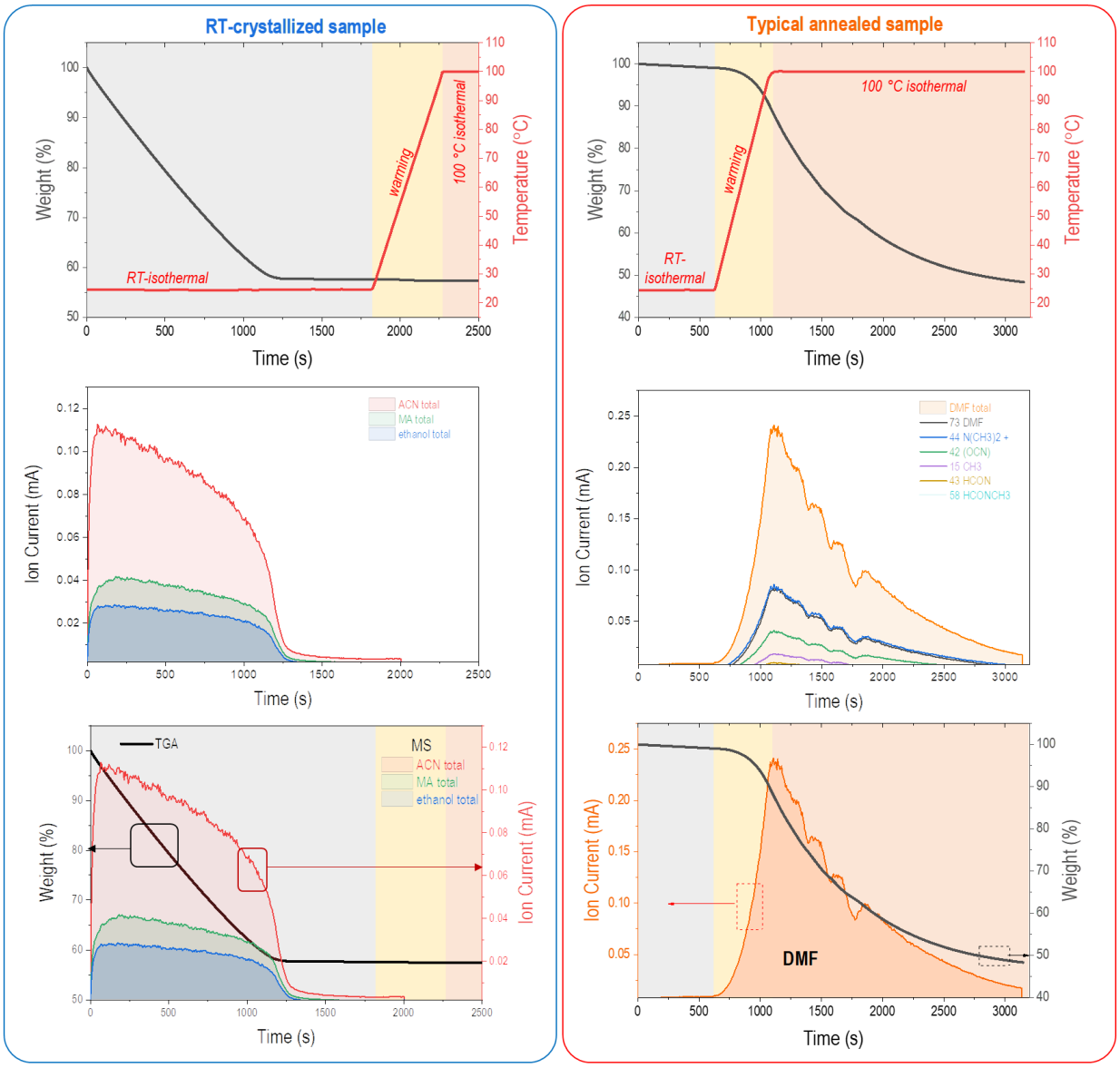

fig. S12 Comparison of TGA-MS results between RT-perovskite and TA-perovskite. RT-perovskite shows rapid evaporation of acetonitrile, methylamine and ethanol at RT and no further components coming out after 1500 s even under annealing at 100 °C. In contrast, TA-perovskite does not show weight loss or solvent evaporation at RT. Only at TA, the nonvolatile solvent DMF starts to come out from the ink and it takes more than 2500 s under a 100 °C annealing to evaporate the DMF.

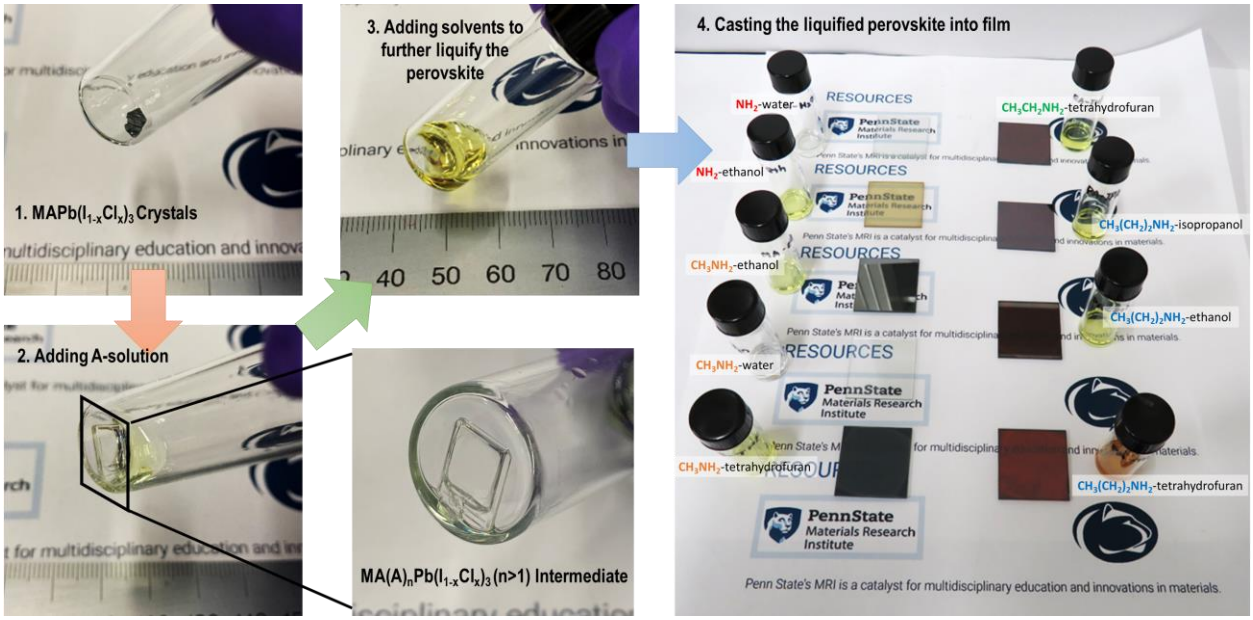

fig. S13 Photograph showing the RT-ink processing procedures, where a single-crystalline intermediate state has been observed (the colorless square crystal has been identified in **Supplementary Note S3**, in conjunction with the XRD data).

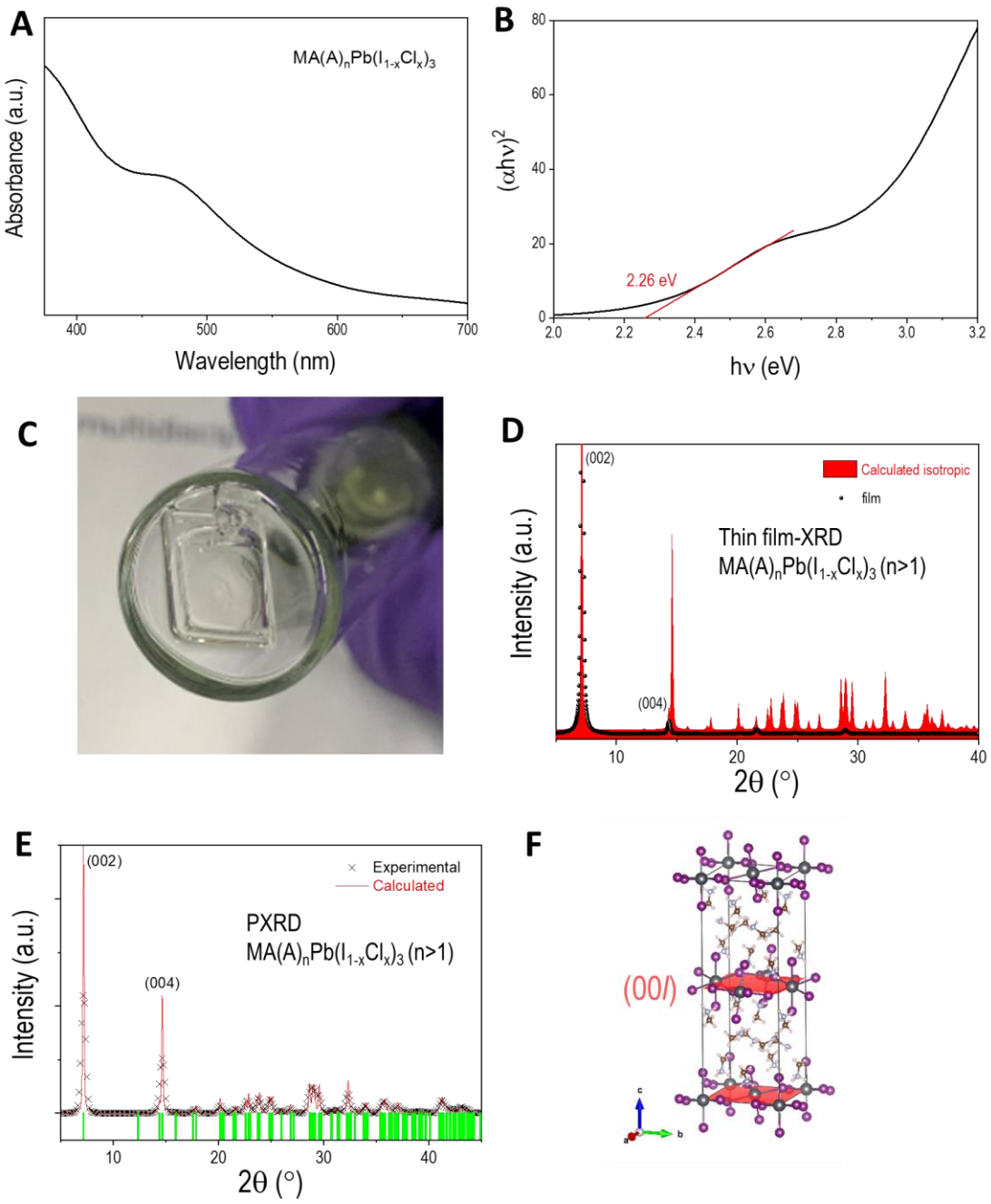

fig. S14 Characterizations on the perovskite intermediate crystal of $MA(A)_nPb(I_{1-x}Cl_x)_3$. (A) UV-vis absorbance spectra. (B) The corresponding Tauc plot. (C) A picture showing the single-crystal of $MA(A)_nPb(I_{1-x}Cl_x)_3$. (D) XRD spectra of a $MA(A)_nPb(I_{1-x}Cl_x)_3$ thin film, displaying strong (00ℓ) orientation. (E) Corresponding PXRD and (F) crystallographic lattice model scheme.

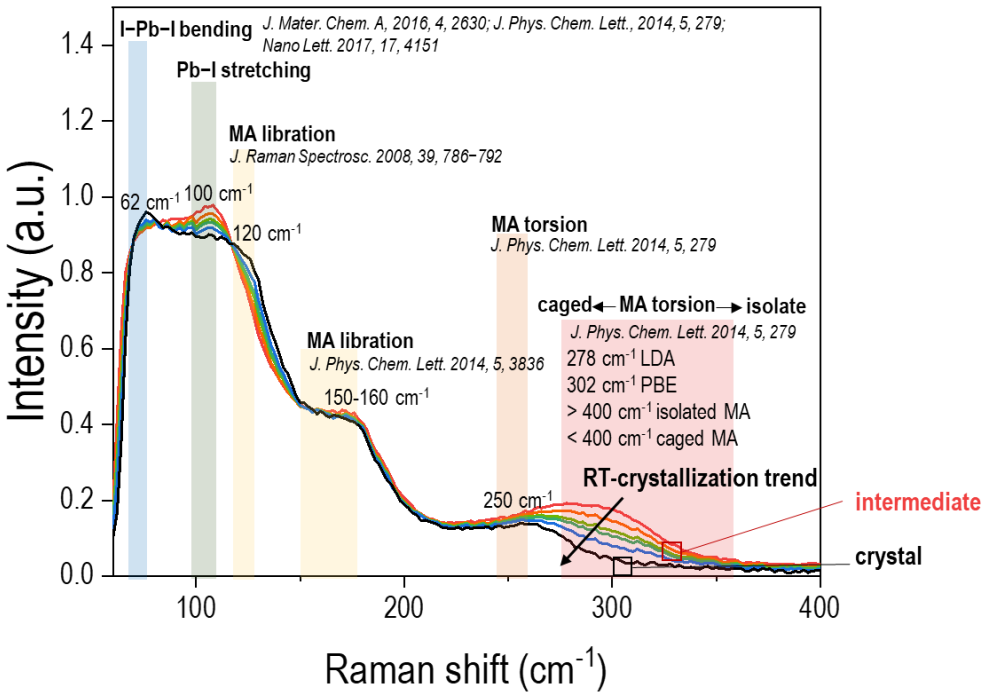

fig. S15 Raman spectral change upon the crystallization of the RT-ink. A RT-crystallization trend is shown to indicate spectral change: starting from an intermediate (red line) to the final crystal (black line). Characteristic peaks are noted with the reference. The low frequency region (60-100 cm^{-1}) is corresponding to the Pb-based octahedral cage, where the lower frequency part (close to 60 cm^{-1}) is related to the "I-Pb-I" bond bending and higher frequency part (close to 100 cm^{-1}) is related to the "Pb-I" bond stretching, respectively. During the RT crystallization process (MA evaporates), the relative intensity ratio between "I-Pb-I" and "Pb-I" bond changes. This suggests that some MA molecules could be involved in the coordination of Pb-centered octahedra, as prior reports have revealed the weak interaction between the N atom (having lone electron pair in alkylamine molecules) and the Pb atom in the octahedra and some other works suggest the MA serves as moderate ligand to coordinate with Pb(II). At higher frequency regions (around 300 cm^{-1}), there is another difference between the intermediate and the final crystal. In the 270-350 cm^{-1} region, the peak gradually shifts towards lower frequency region upon evaporation. In this region, the MA torsion at higher frequency is more related to the isolate MA, which could be the MA in amorphous phase or residual MA in the ink. The MA torsion at lower frequency in this region is more related to the caged MA, as predicted by some prior calculation tools. In the rest frequency regions, MA's torsion (250 cm^{-1}) and libration (150-160 cm^{-1}) are similar in both intermediate and final state.

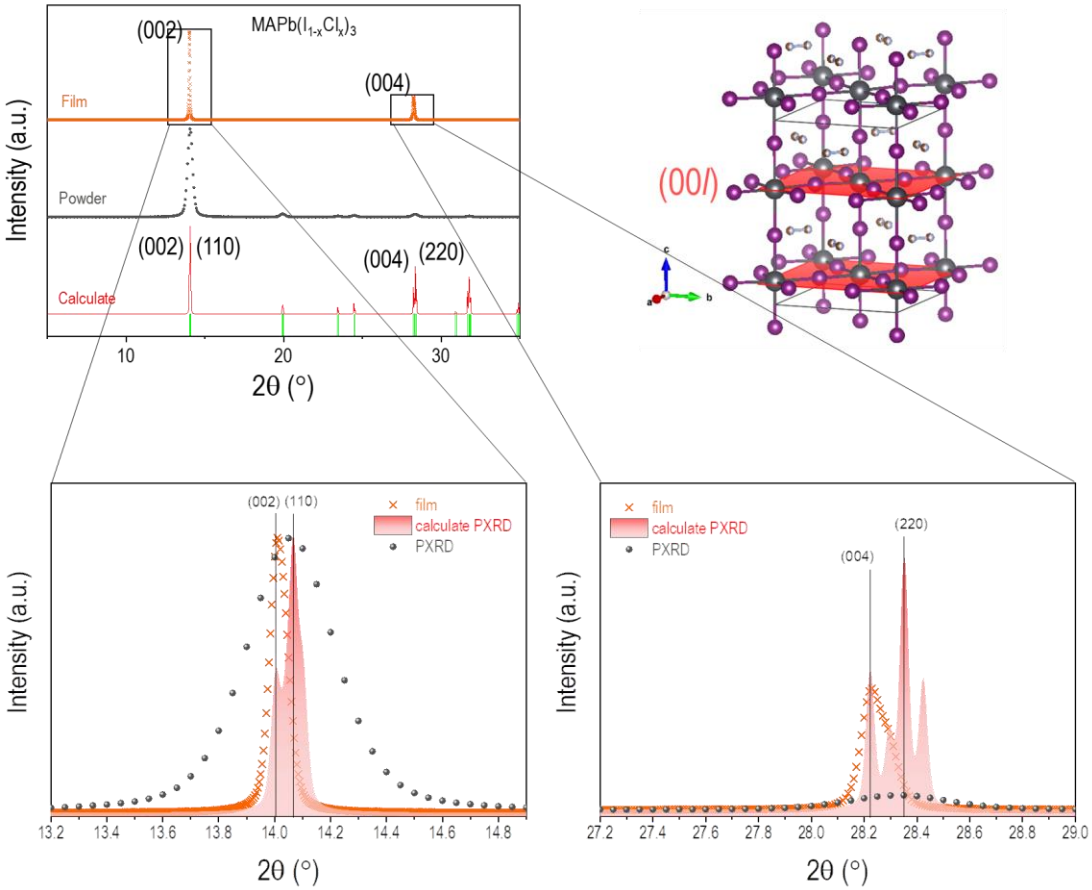

fig. S16 XRD results of the final RT-perovskite film of $MAPb(I_{1-x}Cl_x)_3$, show a strong $\{00\ell\}$ orientation. We calculated the Lotgering factor (LF) from the XRD patterns to quantify the degree of orientation [19], which is 97% for RT-perovskite thin film. The LF, varying from "0" for a non-oriented sample to "1" for a completely oriented sample, is calculated using the equation of $LF = \frac{P-P_0}{1-P_0}$ (where P is the ratio between the summation of the integrated peak intensities corresponding to the preferred orientation planes and the summation of all diffraction peaks and P_0 is the ratio in a randomly orientated sample.

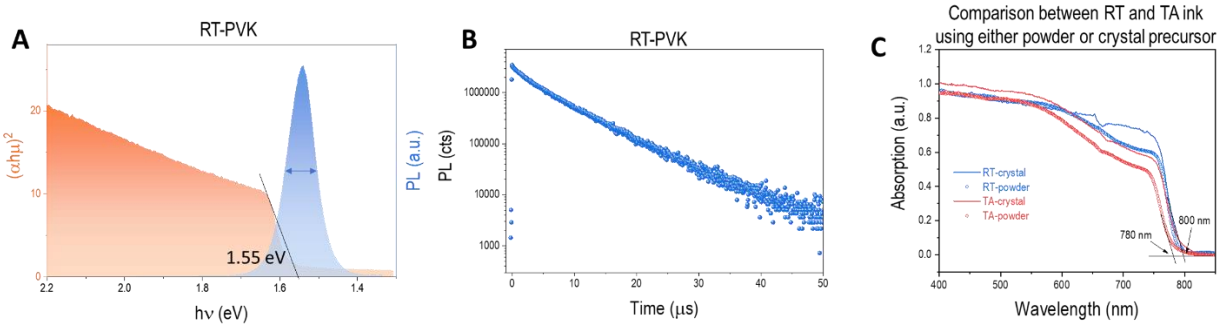

fig. S17 (A) Tauc plot and time-integrated PL of the RT-perovskite thin film (left panel). **(B)** Time-resolved PL of the RT-perovskite thin film (right panel). **(C)** Comparison of UV-vis spectra of films prepared from RT and TA inks, using either powder (mixture of PbI_2, MAI, $PbCl_2$ and MACl powders) or crystal (crystal of $MAPb(I_{1-x}Cl_x)_3$) precursors in the ink.

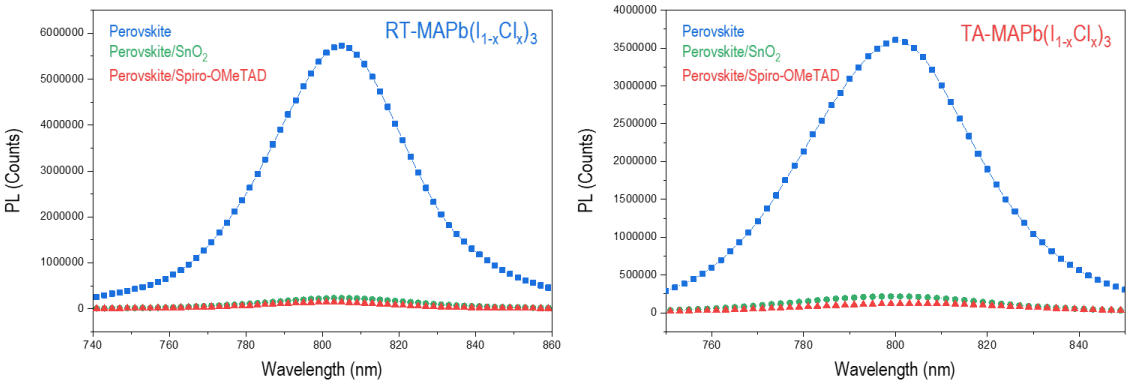

fig. S18 Time-integrated PL of different perovskite films with/without electron/hole quenching layers.

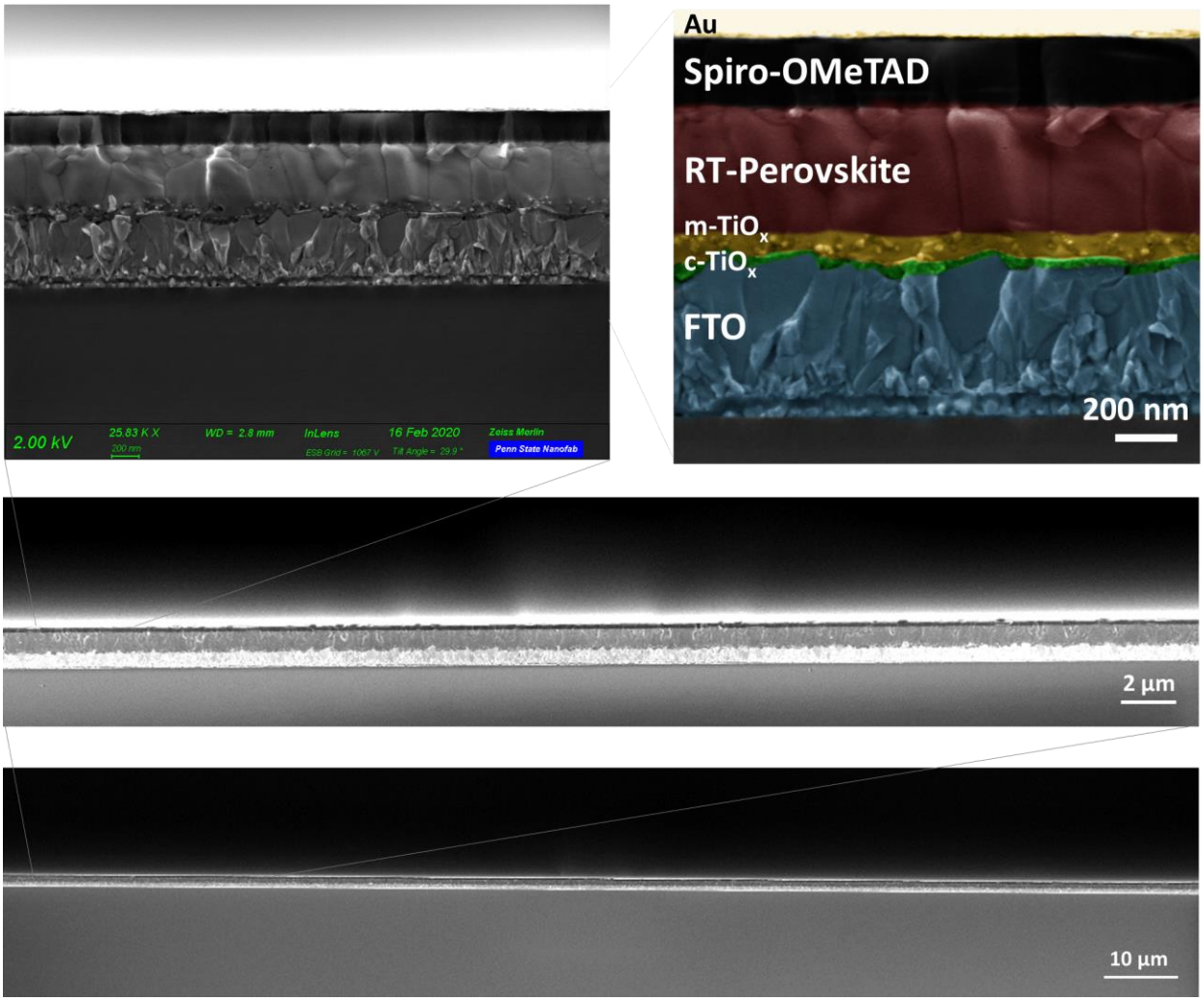

fig. S19 Cross-sectional SEM images showing the **conventional (n-i-p)** structured perovskite solar cell at different magnification scope. Highly homogeneous films with ultra-flat surface can be observed.

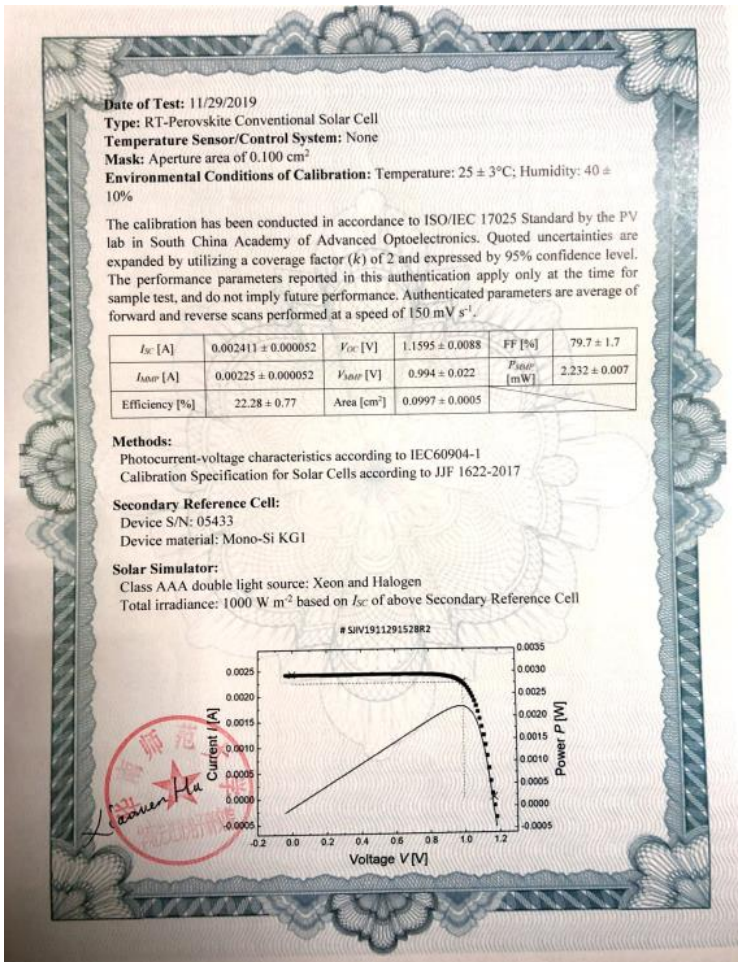

Date of Test: 11/29/2019
Type: RT-Perovskite Conventional Solar Cell
Temperature Sensor/Control System: None
Mask: Aperture area of 0.100 cm^2
Environmental Conditions of Calibration: Temperature: 25 ± 3°C; Humidity: 40 ± 10%

The calibration has been conducted in accordance to ISO/IEC 17025 Standard by the PV lab in South China Academy of Advanced Optoelectronics. Quoted uncertainties are expanded by utilizing a coverage factor (k) of 2 and expressed by 95% confidence level. The performance parameters reported in this authentication apply only at the time for sample test, and do not imply future performance. Authenticated parameters are average of forward and reverse scans performed at a speed of 150 mV s^{-1}.

I_{SC} [A]	0.002411 ± 0.000052	V_{OC} [V]	1.1595 ± 0.0088	FF [%]	79.7 ± 1.7
I_{MAP} [A]	0.00225 ± 0.000052	V_{MAP} [V]	0.994 ± 0.022	P_{MAP} [mW]	2.232 ± 0.007
Efficiency [%]	22.28 ± 0.77	Area [cm^2]	0.0997 ± 0.0005		

Methods:
Photocurrent-voltage characteristics according to IEC60904-1
Calibration Specification for Solar Cells according to JJF 1622-2017

Secondary Reference Cell:
Device S/N: 05433
Device material: Mono-Si KG1

Solar Simulator:
Class AAA double light source: Xeon and Halogen
Total irradiance: 1000 W m^{-2} based on I_{SC} of above Secondary Reference Cell

fig. S20 Independent efficiency authentication from different affiliation: the official authentication report from South China Academy of Advanced Optoelectronics, where the RT-perovskite cell exhibits an efficiency of 22.28%, with a V_{OC} of 1.1595 V, I_{SC} of 0.00241 A and FF of 79.7%.

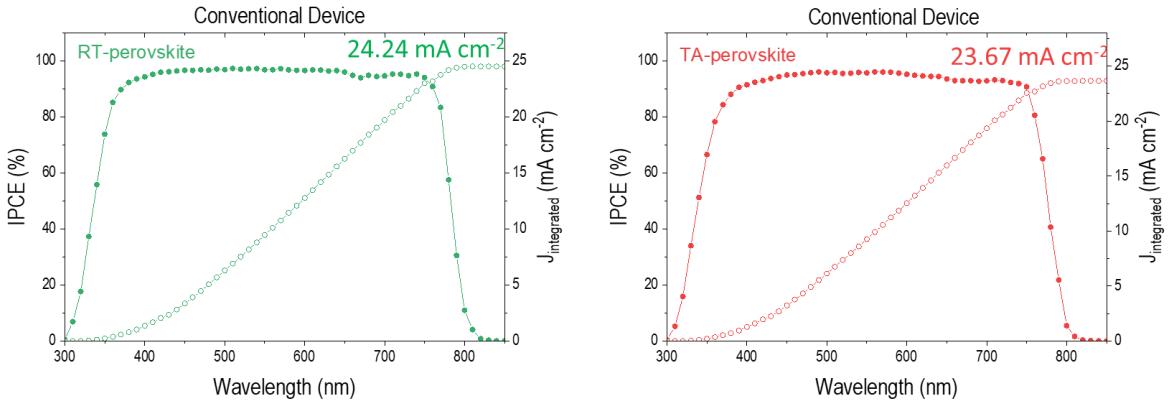

fig. S21 IPCE spectra of **conventional** perovskite solar cells using RT- and TA-perovskite. The current integration is also presented to give a reference number of photocurrents.

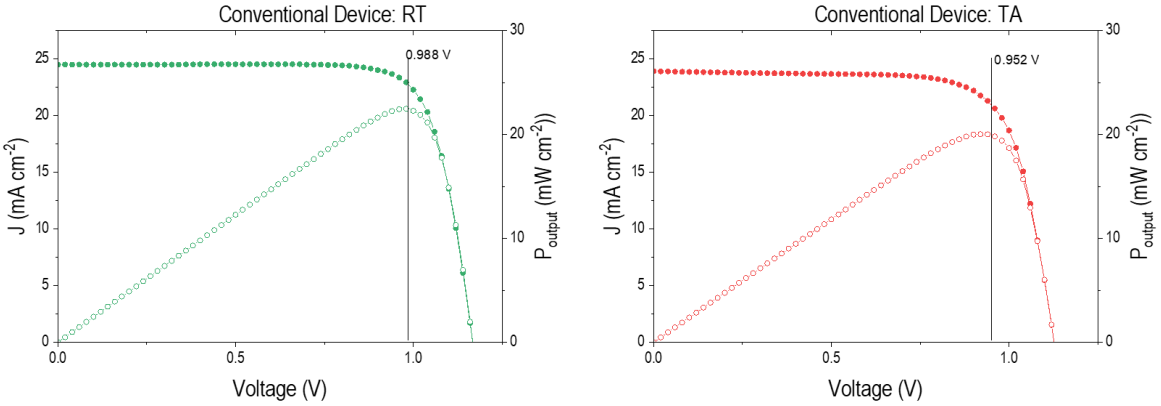

fig. S22 J-V curve and output power-voltage curve of **conventional** perovskite solar cells using RT- and TA-perovskite. The maximal output power point is obtained and noted in each figure.

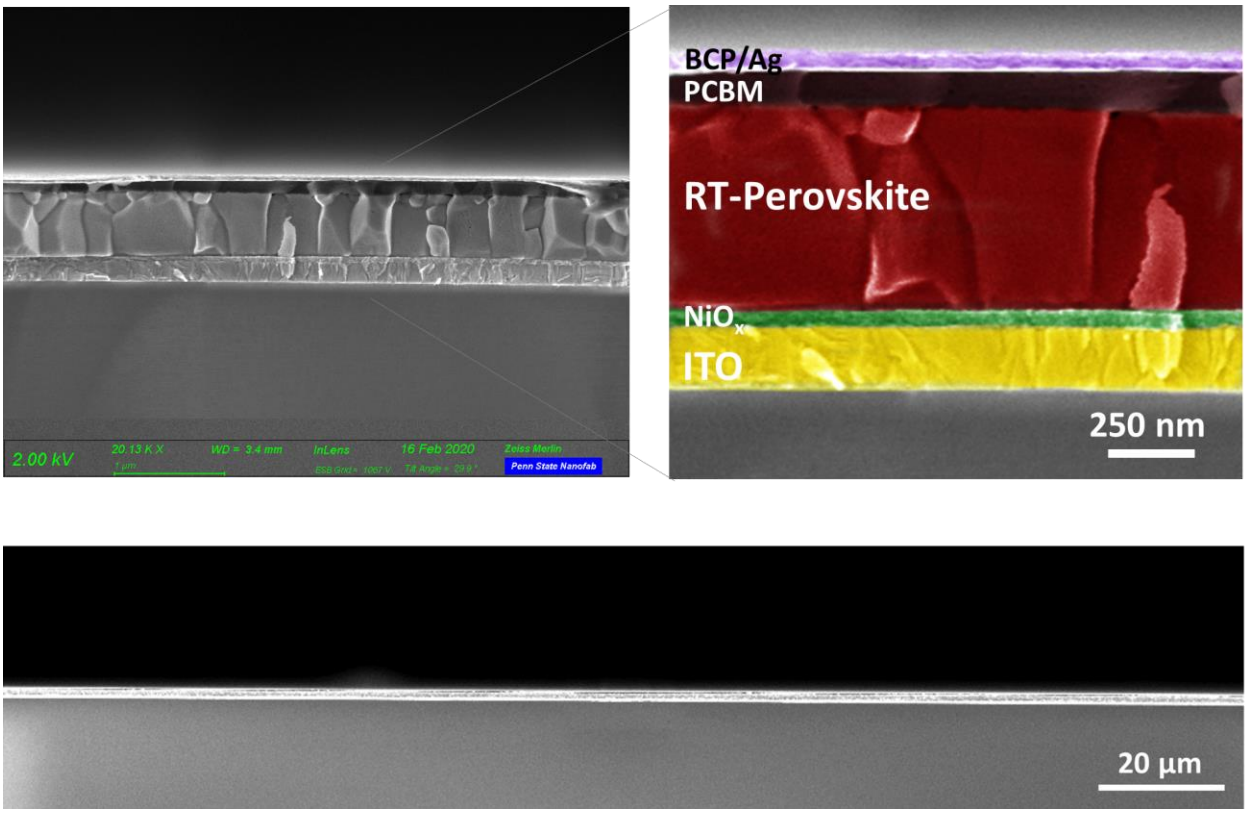

fig. S23 Cross-sectional SEM images showing the **inverted (p-i-n)** structured perovskite solar cell at different magnification scope. Highly homogeneous films with ultra-flat surface can be observed.

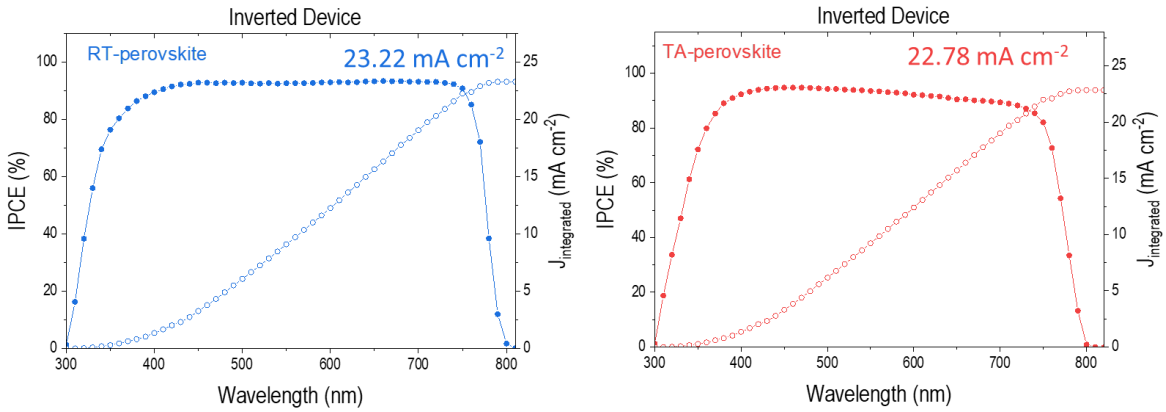

fig. S24 IPCE spectra of **inverted** perovskite solar cells using RT- and TA-perovskite. The current integration is also presented to give a reference number of photocurrents.

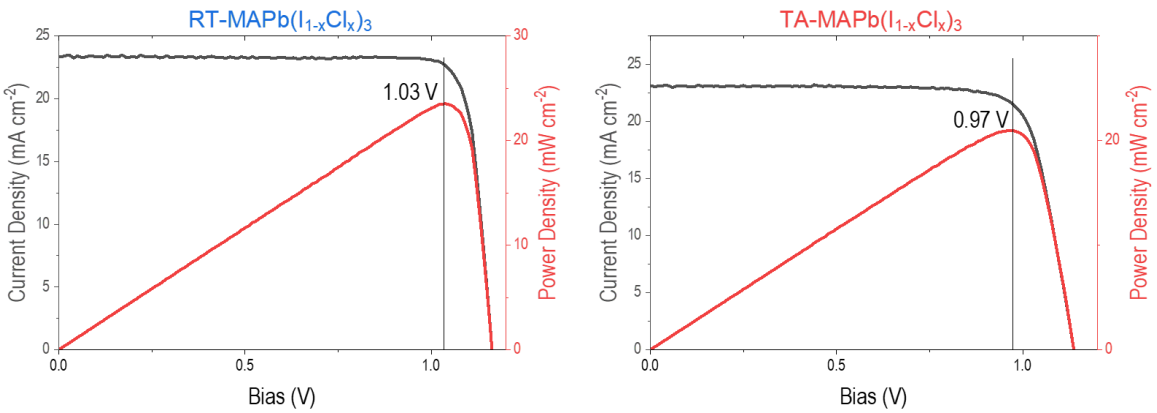

fig. S25 J-V curve and output power-voltage curve of **inverted** perovskite solar cells using RT- and TA-perovskite. The maximal output power point is obtained and noted in each figure.

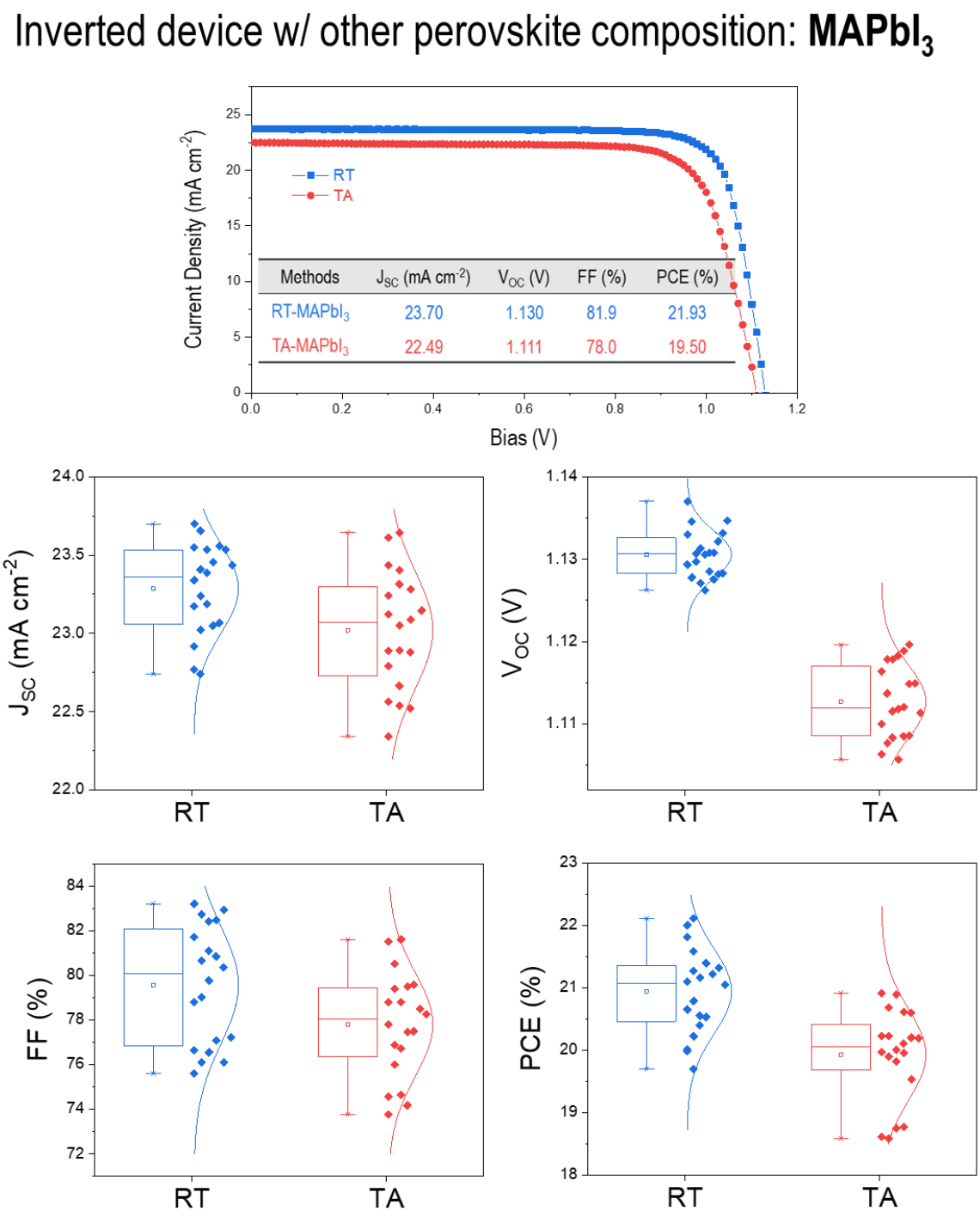

fig. S26 Inverted device performance using alternative perovskite composition: $MAPbI_3$. The RT-device exhibits an average efficiency of 21.93% than that of 19.50% from TA-device. The statistics data also show a narrower distribution of photovoltaic parameters for the RT-device.

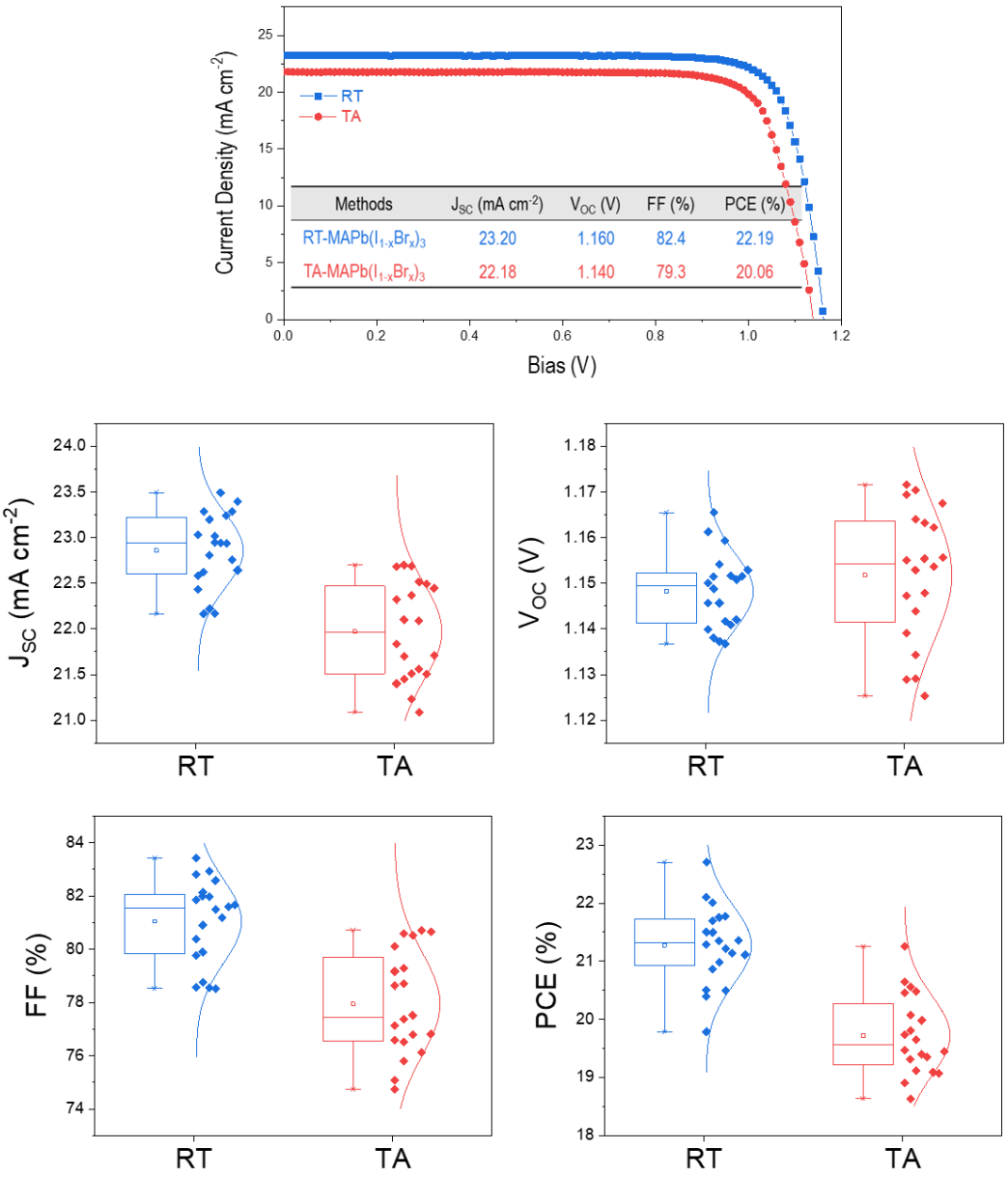

fig. S27 Inverted device performance using alternative perovskite composition: $MAPb(I_{1-x}Br_x)_3$. The RT-device exhibits an average efficiency of 22.19% than that of 20.06% from TA-device. The statistics data also show a narrower distribution of photovoltaic parameters for the RT-device.

Supplementary Tables

Table S3 Fitted TRPL lifetime of RT- and TA- perovskites in the presence and absence of quenching layers, compared with their corresponding charge carrier diffusion length.

Precursor solution	τ (ns)	$\tau_{q,e}$ (ns)	$\tau_{q,h}$ (ns)	$\tau_{q,e}/\tau$	$L_{D,e}$ (nm)	$\tau_{q,h}/\tau$	$L_{D,h}$ (nm)
RT-perovskite	5340.2	18.1	16.9	0.0034	2779	0.0032	2876
TA-perovskite	310.2	10.1	9.4	0.0326	883	0.0303	917

Table S4 Photovoltaic parameters of **conventional (n-i-p)** structured solar cells using RT- and TA- $MAPb(I_{1-x}Cl_x)_3$ perovskite.

Methods	J_{SC} (mA cm^{-2})	V_{OC} (V)	FF (%)	PCE (%)
RT-avg. ± Std.dev.	23.68 ± 0.38	1.149 ± 0.007	78.54 ± 1.03	21.37 ± 0.48
RT-champion	24.38	1.148	80.06	22.40
TA-avg. ± Std.dev.	22.24 ± 0.77	1.113 ± 0.009	76.35 ± 2.02	18.91 ± 0.82
TA-champion	23.96	1.116	75.10	20.08

Table S5 Photovoltaic parameters of 20 individual inverted (**p-i-n**) structured cells using RT-$MAPb(I_{1-x}Cl_x)_3$ perovskite.

J_{SC} (mA cm^{-2})	V_{OC} (V)	FF (%)	PCE (%)
23.45	1.160	84.9	23.09
23.39	1.171	84.6	23.15
22.57	1.153	85.2	22.18
23.11	1.163	82.2	22.08
22.73	1.168	80.8	21.44
23.10	1.147	82.0	21.72
23.28	1.160	80.9	21.85
23.73	1.160	81.9	22.53
23.28	1.161	80.6	21.77
23.36	1.155	81.0	21.85
22.83	1.153	85.2	22.44
23.00	1.156	83.6	22.24
23.83	1.164	81.4	22.59
22.51	1.159	85.1	22.20
22.54	1.148	83.2	21.53
22.25	1.165	84.9	22.01
23.29	1.147	81.0	21.65
22.27	1.149	84.9	21.72
22.37	1.147	84.6	21.70
22.82	1.162	83.2	22.07

Reference (Supplementary Reference, RS)

1 H. Hu, Z. Ren, P. W. K. Fong, M. Qin, D. Liu, D. Lei, X. Lu and G. Li, *Adv. Funct. Mater.*, 2019, **29**, 1900092.

2 Y. Deng, C. H. van Brackle, X. Dai, J. Zhao, B. Chen and J. Huang, *Sci. Adv.*, 2019, **5**, eaax7537.

3 J. W. Jung, S. T. Williams and A. K. Y. Jen, *RSC Adv.*, 2014, **4**, 62971–62977.

4 K. Hwang, Y.-S. Jung, Y.-J. Heo, F. H. Scholes, S. E. Watkins, J. Subbiah, D. J. Jones, D.-Y. Kim and D. Vak, *Adv. Mater.*, 2015, **27**, 1241–1247.

5 A. Y. Alsalloum, B. Turedi, X. Zheng, S. Mitra, A. A. Zhumekenov, K. J. Lee, P. Maity, I. Gereige, A. AlSaggaf, I. S. Roqan, O. F. Mohammed and O. M. Bakr, *ACS Energy Lett.*, 2020, **5**, 657–662.

6 D. Liu, C. Yang, M. Bates and R. R. Lunt, *iScience*, 2018, **6**, 272–279.

7 H. Yu, X. Liu, Y. Xia, Q. Dong, K. Zhang, Z. Wang, Y. Zhou, B. Song and Y. Li, *J. Mater. Chem. A*, 2015, **4**, 321–326.

8 Y. Zhou, M. Yang, W. Wu, A. L. Vasiliev, K. Zhu and N. P. Padture, *J. Mater. Chem. A*, 2015, **3**, 8178–8184.

9 Pin Lu, G. R. Engelhardt, B. Kursten and Digby D. Macdonalda, *J. Electrochem. Soc.*, 2016, **163**, C156–C163.

10 J. F. Kenney and G. W. Willcockson, *J. Polym. Sci. Part A-1 Polym. Chem.*, 1966, **4**, 679–698.

11 S. S. Lim, W. K. Chong, A. Solanki, H. A. Dewi, S. Mhaisalkar, N. Mathews and T. C. Sum, *Phys. Chem. Chem. Phys.*, 2016, **18**, 27119–27123.

12 E. M. Y. Lee and W. A. Tisdale, *J. Phys. Chem. C* 2015, **119**, 9005–9015.

13 M. S. Dresselhaus, *SOLID STATE PHYSICS PART II Optical Properties of Solids*.

14 W. M. (William M. Deen, *Analysis of transport phenomena*, Oxford University Press: New York, NY, 2nd Ed., 2011.

15 J. Mei, M. S. Bradley and V. Bulović, *Phys. Rev. B*, 2009, **79**, 235205.

16 K. Wang, C. Wu, Y. Hou, D. Yang and S. Priya, *J. Mater. Chem. A*, 2019, **7**, 24661–24690.

17 M. Sleutel and A. E. S. Van Driessche, *Proc. Natl. Acad. Sci. U. S. A.*, 2014, **111**, E546–E553.

18 D. Foppiano, M. Tarik, E. Gubler Müller and C. Ludwig, *J. Anal. At. Spectrom.*, 2018, **33**, 1493–1499.

19 F. K. Lotgering, *J. Inorg. Nucl. Chem.*, 1959, **9**, 113–123.